

# Stochasticity in $N$ -body Simulations of Disc Galaxies

J. A. Sellwood<sup>1\*</sup> and Victor P. Debattista<sup>2†</sup>

<sup>1</sup>*Rutgers University, Department of Physics & Astronomy, 136 Frelinghuysen Road, Piscataway, NJ 08854-8019, USA*

<sup>2</sup>*Jeremiah Horrocks Institute for Astrophysics and Supercomputing, University of Central Lancashire, Preston, PR1 2HE, UK*

29 October 2018

## ABSTRACT

We demonstrate that the chaotic nature of  $N$ -body systems can lead to macroscopic variations in the evolution of collisionless simulations containing rotationally supported discs. The unavoidable stochasticity that afflicts all simulations generally causes mild differences between the evolution of similar models but, in order to illustrate that this is not always true, we present a case that shows extreme bimodal divergence. The divergent behaviour occurs in two different types of code and is independent of all numerical parameters. We identify and give explicit illustrations of several sources of stochasticity, and also show that macroscopic variations in the evolution can originate from differences at the round-off error level. We obtain somewhat more consistent results from simulations in which the halo is set up with great care compared with those started from more approximate equilibria, but we have been unable to eliminate diverging behaviour entirely because the main sources of stochasticity are intrinsic to the disc. We show that the divergence is only temporary and that halo friction is merely delayed, for a substantial time in some cases. We argue that the delays are unlikely to arise in real galaxies, and that our results do not affect dynamical friction constraints on halo density. Stochastic variations in the evolution are inevitable in all simulations of disc-halo systems, irrespective of how they were created, although their effect is generally far less extreme than we find here. The possibility of divergent behaviour complicates comparison of results from different workers.

**Key words:** galaxies: evolution – galaxies: haloes – galaxies: kinematics and dynamics – galaxies: spiral

## 1 INTRODUCTION

Miller (1964) pointed out that all gravitational  $N$ -body systems are chaotic, in the sense that the trajectories of all particles in two systems that differ initially by a small shift in the starting position or velocity of even a single particle will diverge exponentially over time. Thus, two simulations started from the same initial conditions will follow identical evolutionary paths only if the arithmetic operations are performed with the same precision and in the same order, so that round off error is identical. These statements are true for every code, irrespective of the algorithm used for the computations, and no matter how many particles are employed. In particular, a simulation can never be reproduced exactly when run with a different code.

Microscopic chaos is unimportant for many applications because the different evolutionary paths of almost identical simulations lead to similar macroscopic properties such as mass profiles, overall shape, *etc.*, which therefore consti-

tute firm results. Binney & Tremaine (2008, hereafter BT08, p. 344) make this argument and cite a test by Frenk *et al.* (1999) which indeed shows that many different codes yield similar key properties after following the collapse of a dark matter halo. In fact, results generally converge in tests that vary the numerical grid, softening, and/or number of particles (*e.g.* Power *et al.* 2003; Diemand *et al.* 2004), which they would not do if there were a large element of stochasticity. Sellwood (2008) also demonstrated exquisitely reproducible evolution of halo models that were perturbed by externally imposed bars, in sharp contrast to the results presented here.

Simulations with active discs of particles, on the other hand, are not so well behaved. Sellwood & Debattista (2006) reported some minor differences, and one major, in a set of experiments using different numerical parameters but the same file of initial coordinates. We show here that simulations with discs can, at least for certain models, exhibit bimodally divergent macroscopic results, even between cases that differ only at the round-off error level. The reason for this qualitative difference for discs is because collective instabilities and vigorous responses develop from particle noise.

\* E-mail: sellwood@physics.rutgers.edu

† E-mail: vpdebattista@uclan.ac.uk

Here we identify a number of distinct causes of stochastic behaviour in discs, and demonstrate explicitly how the evolution is affected.

We show that the principal sources of divergent behaviour are: (a) multiple in-plane global modes, (b) swing amplified noise, (c) bending instabilities, (d) suppression of dynamical friction, and (e) the truly chaotic nature of  $N$ -body systems. We also show that the distribution of evolutionary paths taken in simulations of different realizations of the same model varies systematically with the care taken to set up the initial coordinates of halo particles.

We deliberately choose to illustrate just how large the differences can be for one particular unstable equilibrium model. Stochasticity is present in all simulations and its effects are always noticeable in those containing discs, but generally variations in the evolution show less scatter than in the case studied here. We show that the range of behaviour is similar in two quite distinct  $N$ -body codes and illustrate the sensitivity to differences at the round-off error level. We also show that increasing the number of particles does not reduce the spread of measured properties.

Real galaxies are assembled and evolve in a complicated manner, and certainly do not pass through a well-constructed axisymmetric, equilibrium phase that is unstable, although such a model is commonly used as a starting point of simulations. The objectives of experiments of this type are therefore (1) to determine whether plausible axisymmetric galaxy models are globally stable and (2) to develop an understanding of the dynamical evolution of models that form bars and other non-axisymmetric structures. While we adopt a model of this type in this paper, its remarkable behaviour has implications for all simulations of disc-halo models, regardless of how they were created.

The main part of the paper demonstrates the role of the five above-named sources of stochasticity in the evolution of disc models. We also explicitly show the effects of different particle selection techniques on the robustness of the behaviour. Stochastic divergence has been reported elsewhere, but not recognized as an intrinsic aspect of these models; *e.g.*, Klypin *et al.* (2008) attributed divergent evolution to inadequate numerical care, whereas stochasticity could be the cause. Appendix B reports extensive tests that confirm that the results we report here do not depend on any numerical parameters.

## 2 SELECTION OF PARTICLES

The selection of initial particle positions and velocities of an equilibrium model requires careful attention. Random selection of even many millions of particles will lead to shot noise variations in both the density and velocity distributions of a model. Here we summarize the available techniques to select initial coordinates of particles, with a focus on disc-halo models. These methods generally yield a set of particles that are not specific to any particular  $N$ -body code.

### 2.1 Selecting from a DF

Jeans theorem requires that an equilibrium model should have a distribution function (DF) that is a function of the isolating integrals (BT08, p. 283). Thus the best way to

realize an equilibrium set of particles for an initial model is to select from a DF, when one is available.

While random selection of particles may be common practice, it immediately discards a large part of this potential advantage. One widely used technique (*e.g.* Holley-Bockelmann *et al.* 2005; Weinberg & Katz 2007; Zhang & Magorrian 2008; Dubinski *et al.* 2009) is to accept or reject candidate particles based on a comparison of a random variable with the value of the DF at the phase-space position of each particle, which introduces shot noise in the density of particles in integral space. The evolution of the simulation will be that of the selected DF, not the intended one, and different random realizations lead to significant variations in the measured frequencies of the instabilities in the linear regime (Sellwood 1983) and substantial differences in the non-linear regime. It is therefore best to adopt a deterministic procedure for particle selection from a DF.

A scheme to select particles smoothly in this way, first used in Sellwood (1983) and described more fully in Sellwood & Athanassoula (1986), is summarized in the Appendix of Debattista & Sellwood (2000). We divide integral, generally  $(E, L)$ , space into  $n$  areas in such a way that  $\int \int F dE dL$  over each small area is exactly  $1/n$ th of the integral over the total accessible ranges of  $E$  &  $L$ . Here  $F(E, L)$  is the differential distribution after integration over the other phase space variables (BT08, pp. 292, 299). Requiring that one particle lies within each area ensures that the selected set of particles is as close as possible to representing the desired particle density in integral space. We choose the precise position of a selected particle within each area quasi-randomly in order to ensure that the particles do not lie on an exact raster in integral space. We describe this scheme as deterministic selection from the DF, a term that ignores this minor random element.

This scheme is readily adapted to select particles of unequal masses if desired. To select particles having masses proportional to a weight function  $w(E, L)$ , one simply weights the DF by  $w^{-1}$ , which automatically adjusts the subdivision of  $(E, L)$ -space into areas of equal weighted DF, as described in Sellwood (2008).

The phases of the particles around the orbit defined by these integrals can be selected at random. We have no evidence that the choice of radial phase, either for flat discs or for spheres, causes significant variations in the outcome and we discuss the choice of azimuthal phases in Section 2.3 below.

Debattista & Sellwood (2000) describe the similar procedure for 2-integral spheroidal models.

### 2.2 When No Simple DF Is Available

Comparatively few useful mass models have known DFs, and the realization of an equilibrium set of particles for a general model presents a significant challenge. Some authors (*e.g.* Shlosman & Noguchi 1993) have simply created a rough  $N$ -body system, which they then evolve in the presence of a frozen disc, thereby allowing the halo to relax towards some nearby equilibrium.

Hernquist (1993) advocates solving the Jeans equations for each component in the combined potential of all mass components. His method is widely

used (*e.g.* Valenzuela & Klypin 2003; Athanassoula 2003; El-Zant *et al.* 2004; Klypin *et al.* 2008), but the resulting equilibrium is approximate.

In general, it is better to derive an approximate DF for a spherical or spheroidal system. An isotropic DF for a spherical system can usually be obtained by Eddington inversion (BT08, p. 289), although it is important to verify that the function is positive for all energies (which it generally is, for reasonable mass models).

Creating an equilibrium DF for a multi-component system presents a greater challenge, for which three effective approaches have been developed. Raha *et al.* (1991), Kuijken & Dubinski (1995) and Debattista & Sellwood (2000) employ the method of Prendergast & Tomer (1970) to derive the mass distribution for a halo having some assumed DF that will be in equilibrium in the presence of one or more other mass components. Alternatively, one can use Eddington’s inversion formula for the halo only in the potential of the combined disc and halo (Holley-Bockelmann *et al.* 2005). A third possibility, as here, is to start from a known spherical halo with a known DF and compress it by adding a disc and/or a bulge using Young’s (1980) method (see Sellwood & McGaugh 2005), and then to select particles from the compressed DF. Even though the last two methods use only the monopole term for the disc, all three methods yield a spheroidal system that is close to detailed equilibrium everywhere.

In general, it is more difficult to construct a good equilibrium for a disc component. The circular speed in the disc mid-plane as a function of radius is determined by the total mass distribution and, commonly, one specifies  $Q(R)$  (Toomre 1964) to determine the radial velocity spread at each radius. The Jeans equations in the epicycle approximation (BT08, p. 326) generally yield a poor equilibrium except when the radial dispersion is a small fraction of the circular speed, and the asymmetric drift formula may have no solution near the centres of hot discs. Shu (1969) describes an approximate DF for a warm disc with a given radial velocity dispersion that we, and Kuijken & Dubinski (1995), have found to be quite serviceable. Again in cases where the radial velocity dispersion stretches the validity of the epicycle approximation, radial gradients can lead to a disc surface density after integration over all velocities that differs slightly from that specified, as shown in Section 3.1.

The vertical structure of an isothermal stellar sheet is given by the formulae developed by Spitzer (1942) and Camm (1950), and BT08 (p. 321) describe a generalization of the in-plane DF to include this feature, which they describe as the Schwarzschild DF. The Spitzer-Camm formulae assume full Newtonian gravity and no radial density or dispersion gradient. Force softening has an increasingly detrimental effect on the vertical balance as the ratio of disc thickness to softening length is reduced, we therefore prefer to construct a vertical equilibrium from the 1D vertical Jeans equation in the actual force field of the softened disc potential, which leads to a better equilibrium.

### 2.3 Quiet Starts

The quiet start technique is a valuable addition to the set up process only when the model has a few vigorous, large-scale instabilities, such as arise in a cool, massive disc with a rota-

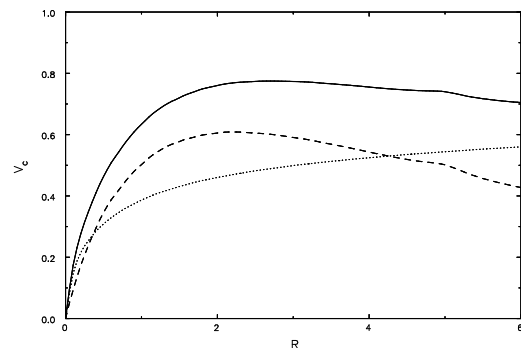


**Figure 1.** The inner rotation curve of our standard model (solid). The separate contributions of the disc (dashed) and halo (dotted) are also shown.

tion curve that rises approximately linearly from the centre. It is of little help when linear stability theory predicts the model to be responsive but (almost) stable (*e.g.* Sellwood 1989; Sellwood & Evans 2001). In these latter cases, collective responses to residual noise grow more vigorously than any global modes, and the particle arrangement randomizes quickly.

For a quiet start, one reproduces each selected master particle multiple times in a symmetrical arrangement, with image particles having the identical radius and velocity components in polar coordinates. We restrict the meaning of the phrase “quiet start” to this symmetrical arrangement of particles – *i.e.* a quiet start can be used no matter how the coordinates of the master particles are selected. Conversely, a “noisy start” means only that azimuthal coordinates are selected at random, again independent of how the master particles are selected. The procedures for discs and spheroidal components differ slightly.

For discs, we place image particles at the corners of an almost regular polygon in 2D, centred on the model centre. The polygon is not exactly regular because we nudge the particles away from exact  $n$ -fold symmetry by a random fraction of a small angle, typically  $0.02^\circ$ . When the disc has a finite thickness, the polygon must be duplicated with a second on the opposite side of the mid-plane for which both the vertical position  $z$  and velocity  $v_z$  of every particle in each of the two polygons have opposite signs.

When the force-determination method is based around an expansion in sectoral harmonics that is truncated at low order,  $m_{\max}$ , and the number of sides to the polygon  $n \geq 2m_{\max} + 1$ , azimuthal forces in the initial model are much lower than would arise from particle shot noise – hence the label “quiet start”.

We have not tried quiet starts for other force methods, but they could still offer a significant advantage provided that the number of corners adopted for the polygon exceeds the azimuthal order of all the strong instabilities and non-axisymmetric responses (Section 5.3) by at least a factor two.

We adopt a similar procedure for spheroidal components, except that we create image particles by rotating the initial position and velocity vectors using the usual rotation matrix for the adopted set of Euler angles (*e.g.* Arfken 1985, p. 199). The set of Euler angles used creates an  $n$ -fold rotationally symmetric set of particles, which is also reflection

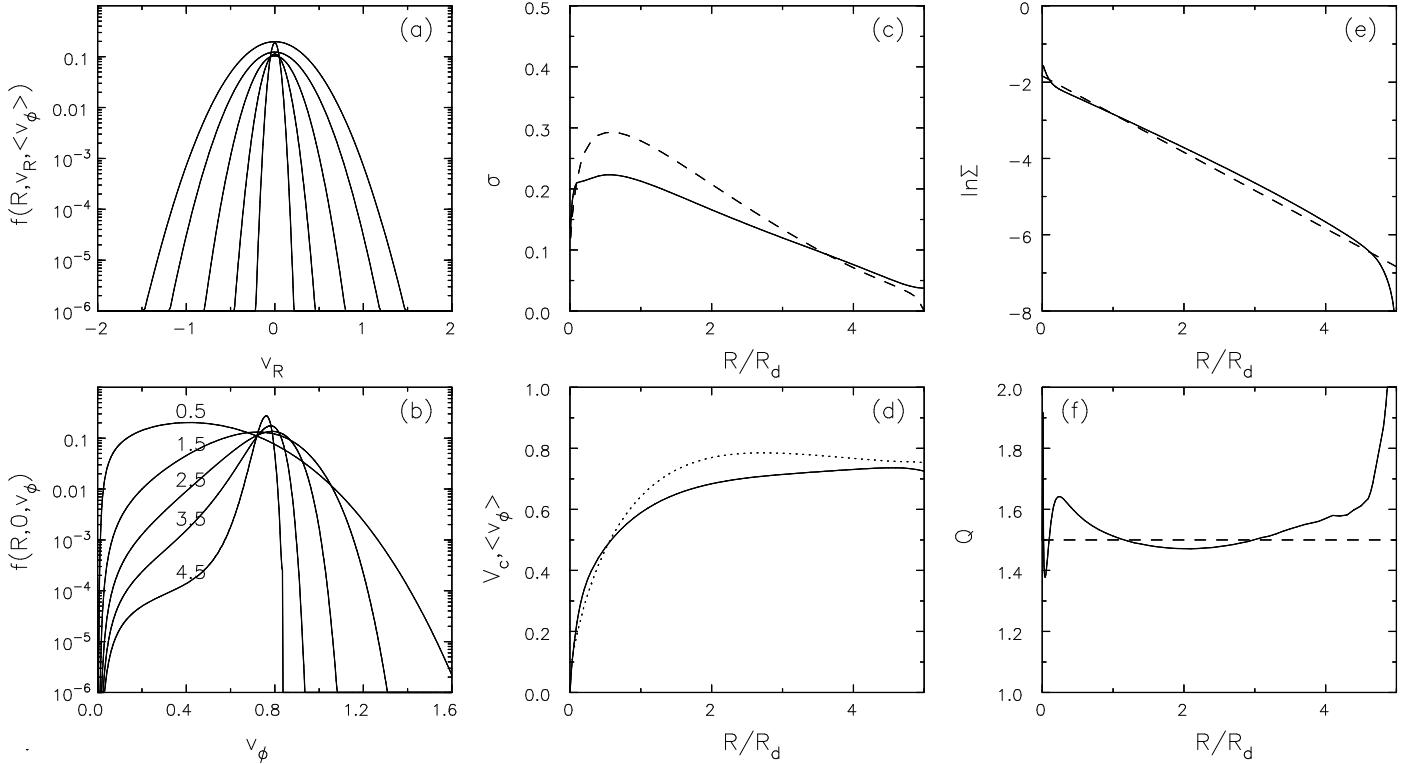


**Figure 2.** Details of the approximate DF for the disc. Panels (a) and (b) show respectively the variation of  $f$  with radial velocity and azimuthal velocity at five different radii. Panel (c) shows the radial variations of the rms azimuthal speed ( $v_\phi$ , solid) and radial speed ( $v_r$ , dashed), (d) compares the circular speed (dotted) with the mean  $v_\phi$  (solid) to illustrate the asymmetric drift. Panels (e) and (f) compare respectively the actual surface density and  $Q$  profiles (solid) with the desired profiles (dashed). The DF does not reproduce these curves perfectly, but the departures are minor.

symmetric about the mid-plane, and has zero net momentum with a centre of mass at the model centre; each master particle is therefore inserted  $2n$  times. It is reasonable to adopt  $n \gtrsim 4$ .

### 3 MODELS

Here we describe all the various galaxy models we use in this paper.

#### 3.1 Standard Galaxy Model

Our standard model is a composite disc-halo system with the rotation curve shown in Fig. 1. The two mass components are an exponential disc and a compressed, strongly truncated, Hernquist halo.

The initial surface density of the disc has the usual exponential form

$$\Sigma(R) = \frac{M_d}{2\pi R_d^2} e^{-R/R_d}, \quad (1)$$

where  $M_d$  is the nominal disc mass. We truncate the disc at  $R = 5R_d$ , leaving an active disc mass of  $\approx 0.96M_d$ . The disc particles are set in orbital motion with a radial velocity spread so as to make Toomre's  $Q = 1.5$ . For most models, we determine the approximate equilibrium velocities by solving the Jeans equations in the epicycle approximation as described in Section 2.2.

In some cases we adopt Shu's approximate DF instead, and select disc particles deterministically from it. Properties of the DF and the radial variations of the low-order velocity moments are shown in Fig. 2. While the radial velocity distributions are nicely Gaussian, the azimuthal velocity distributions (2b) are markedly skewed. This aspect, and the departures of the surface density and  $Q$  profiles from the desired values all decrease for models with less dominant discs or with lower values of  $Q$ .

For fully 3D simulations, the density profile normal to the disc plane is Gaussian, with a constant scale height of  $0.05R_d$  and appropriate vertical velocities in the numerically determined vertical force profile.

We construct a halo in equilibrium with the disc in the following manner. We start from the initial density profile suggested by Hernquist (1990)

$$\rho_0(r) = \frac{M_h r_s}{2\pi r(r_s + r)^3}, \quad (2)$$

which has total mass  $M_h$  and scale radius  $r_s$ , with the isotropic distribution function (DF) also given by Hernquist. We strongly truncate this halo by eliminating all particles with enough energy to reach  $r > 2r_s$ , causing the density to taper gently to zero at this radius, and an actual halo mass of  $\approx 0.25M_h$ . Since most of the discarded mass is at large radii, there is little change to the central attraction at  $r < 2r_s$  and the model remains close to equilibrium.

For our standard model, we choose  $r_s = 40R_d$  and set  $M_h = 80M_d$  so that the halo mass is approximately 19 times

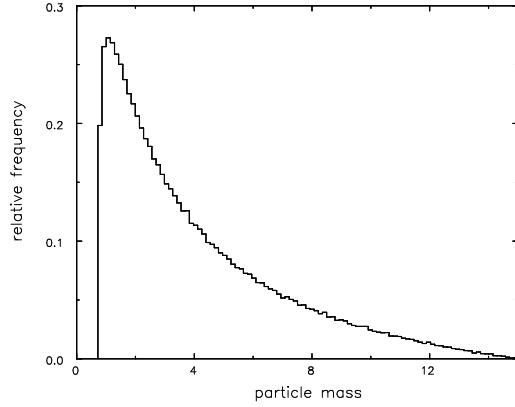


**Figure 3.** The frequency distribution of halo particle masses, in units of the disc particle mass.

that of the disc. We then employ the halo compression algorithm described by Sellwood & McGaugh (2005) to compute a new, mildly anisotropic, DF for the compressed halo that results from including the above disc. The rotation curve, Fig. 1, shows that the disc dominates the central attraction over most of the inner part and the total rotation curve is approximately flat at large radii.

We adopt a system of units such that  $G = M_d = a_d = 1$ , where  $G$  is Newton’s constant,  $M_d$  is the mass of the untruncated disc, and  $a_d$  is the length scale for the type of disc adopted. Therefore distances are in units of  $a_d$ , masses are in units of  $M_d$ , one dynamical time  $\tau = (a_d^3/GM_d)^{1/2}$ , and velocities are in units of  $\hat{v} = (GM_d/a_d)^{1/2} \equiv a_d/\tau$ . One possible scaling to physical units is to choose the dynamical time to be 10 Myr and  $a_d = 3$  kpc, which implies  $M_d = 5.98 \times 10^{10} M_\odot$ . The velocity unit  $\hat{v} = 293 \text{ km s}^{-1}$ , and the peak circular speed in Fig. 1 is approximately  $235 \text{ km s}^{-1}$ .

We also present results for two other disc-halo models for which we choose  $r_s = 30R_d$  and  $r_s = 50R_d$ , *i.e.* that bracket our standard case. The more extended halo leads to a more dominant disc, while the disc is less dominant in the more concentrated halo.

We select halo particles from the compressed DF using the smooth procedure summarized in Section 2.1, with the weight function for particle masses being  $w(L) = 0.5 + 20L$ , where  $L = |\mathbf{L}|$  is the total specific angular momentum. All disc particles have equal masses, but the masses of halo particles range from 0.7 to 14.6 times the mass of the disc particles. Fig. 3 shows the frequency distribution of halo particle masses.

As a result of this careful procedure, both the disc and halo components are very close to equilibrium in the combined potential and the initial ratio of kinetic to the virial of Clausius (measured from the particles) is  $T/|W| = 0.498$ . At the same time, the phases of the particles in their carefully selected orbits are chosen at random, so that the model indeed starts from the usual level of shot noise resulting from the random locations of the particles.

### 3.2 Isochrone Disc

We also present results using the isochrone disc with no halo. The potential (BT08, p. 65) has a simple form

**Table 1.** Numerical parameters for our standard runs

	Cylindrical grid	Spherical grid
Grid size	$(N_R, N_\phi, N_z)$ $= (127, 192, 125)$	$n_r = 500$
Angular compnts	$0 \leq m \leq 8$	$0 \leq l \leq 4$
Outer radius	$6.076R_d$	$80R_d$
$z$ -spacing	$0.01R_d$	
Softening rule	cubic spline	none
Softening length	$\epsilon = 0.05R_d$	
Number of particles	500 000	2 500 000
Equal masses	yes	no (see Fig. 3)
Shortest time step	$0.0125(R_d^3/GM)^{1/2}$	$0.0125(R_d^3/GM)^{1/2}$
Time step zones	5	5

$$\Phi(R) = -\frac{GM_d}{a} \left[ x + (1 + x^2)^{1/2} \right]^{-1}, \quad (3)$$

while the surface density is

$$\Sigma(R) = \frac{M_d a}{2\pi r^3} \left\{ \log \left[ x + (1 + x^2)^{1/2} \right] - \frac{x}{(1 + x^2)^{1/2}} \right\}. \quad (4)$$

Here  $a$  is a length scale, and  $x = r/a$ ; note  $\Sigma(0) = M_d/(6\pi a^2)$ . Kalnajs (1976) describes a convenient family of DFs characterized by a parameter  $m_K$ ; we refer to each model as the isochrone/ $m_K$  disc. He (Kalnajs 1978) also presents some preliminary results for the normal modes, which were confirmed in simulations (Earn & Sellwood 1995). The local stability parameter (Toomre 1964) for the isochrone/5 disc has a near constant value of  $Q \simeq 1.6$ , and is  $Q \simeq 1.2$  for the isochrone/8 model.

## 4 RESULTS

We begin by showing just how much variation can occur. We first present the evolution of our standard disc/halo model whose rotation curve is shown in Fig. 1. Note that the disc equilibrium in these models is set by solving the Jeans equations, while the halo particles are selected deterministically from a DF. Fig. 4 shows results from 16 separate runs with Sellwood’s (2003) hybrid grid code using fixed numerical parameters, given in Table 1, but with different random seeds for the initial coordinates of the disc particles only. We plot the evolution of both the amplitude and pattern speed of the bar, measured as described in Appendix A. Even though the initial particles are selected from the same distributions, with different random seeds for the disc only, the amplitude evolution differs greatly from run to run and there is considerable spread in the evolution of the pattern speed.

In order to demonstrate immediately that the scatter in Fig. 4 is not a numerical artefact of our grid code, Fig. 5 shows the results of a similar test with 5 runs using the tree code PKDGRAV (Stadel 2001) using an opening angle  $\theta = 0.7$ . PKDGRAV is a multi-stepping code, with time steps refined such that  $\delta t = \Delta t/2^n < \eta(\epsilon/a)^{1/2}$ , where  $\epsilon$  is the softening and  $a$  is the acceleration at a particle’s current position. We use base time step  $\Delta t = 0.01$  and  $\eta = 0.2$ , which gives identical time steps for all particles. The results show a comparable spread in the evolution of both the amplitude and pattern speeds. Results from the two codes with identical initial coordinates for all the particles do not compare in detail. For this problem, the tree code runs about

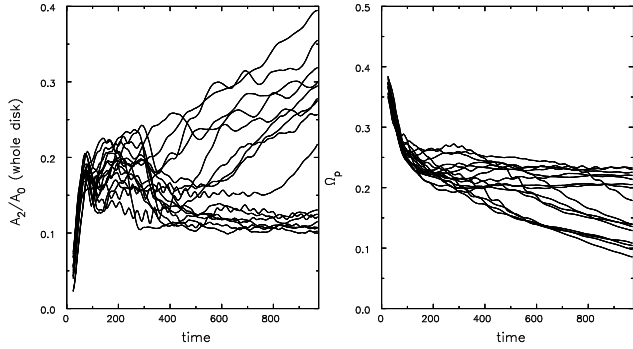


**Figure 4.** Evolution of the amplitude (left) and pattern speed (right) of the bar in 16 runs with different random seeds for the disc particle coordinates, run using Sellwood’s (2003) hybrid code. The tiny differences in the initial models lead to a remarkably wide range of properties of the bar at late times.

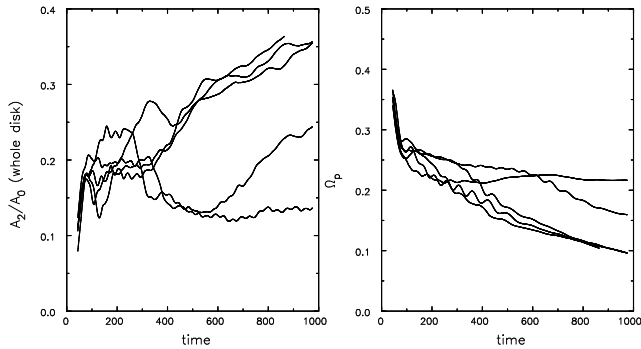


**Figure 5.** Evolution of 5 runs with different random seeds for the disc particle coordinates, run using PKDGRAV with  $\epsilon = 0.05R_d$ .

37 times more slowly than Sellwood’s (2003) grid code; we therefore use it only for this cross check.

The gross qualitative behaviour of all the models in Figs. 4 & 5 is similar at first. The bar forms at similar times with similar pattern speeds, though the initial peak amplitude varies by about  $\sim 25\%$ . The evolution thereafter further diverges, notably with increasingly large differences in the bar amplitude. Steep declines in the bar amplitude in the interval  $200 \lesssim t \lesssim 400$  are generally associated with buckling events (*e.g.* Raha *et al.* 1991), but the timing of these events varies considerably. At late times in Fig. 4, the bar amplitude rises steadily in 9/16 simulations, although starting from different times in each case, while it stays low (over the time interval shown) in the remaining 7.

It is more encouraging to note that the rate of decrease of the bar pattern speed does correlate with the bar amplitude; strong bars are more strongly braked by halo friction, as expected. Furthermore, continued amplitude growth of bars that are strongly braked has been reported previously (*e.g.* Athanassoula 2002).

#### 4.1 Divergence at Late Times

Dubinski *et al.* (2009) report a similar study of bar-unstable disc-halo models, which also reveal large amplitude differences in the short term. However, they stress that the long-

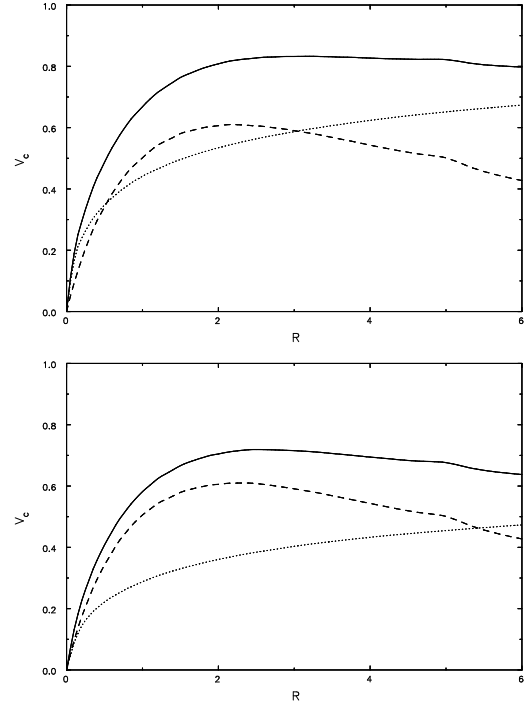


**Figure 6.** The inner rotation curves of models with (above) a slightly more dominant halo and (below) a slightly more extended halo. The line styles mean the same as in Fig. 1. The behaviour of these models is shown in Figs. 7 & 8

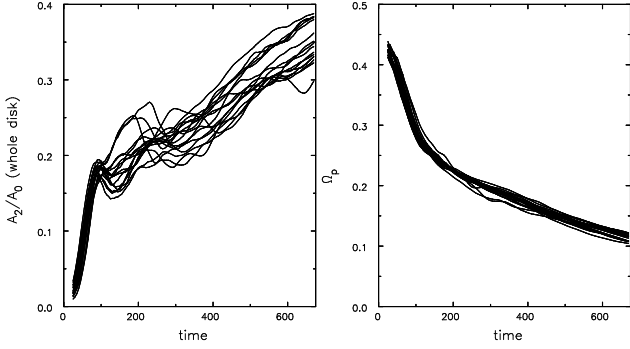
term evolution of their simulations is reproducible, in contrast to our finding.

Fig. 7 shows that we confirm their conclusion for a different model with a slightly more dominant halo; the evolution of both the bar amplitude and pattern speed shows much less scatter than is seen in Fig. 4. All cases show a steady rise in bar amplitude after the buckling event, although the curves for the different realizations during this stage of the evolution are offset in time, as also found by Dubinski *et al.*

Fig. 8 shows results from a third model with a more dominant disc. The amplitude evolution in this model is again bi-modal, rising steadily at late times in half the cases, although not by as much as in our standard case (Fig. 4). The rotation curves of both these models are shown in Fig. 6.

The late rise in bar amplitude occurs, if at all, only in models with live haloes and is associated with frictional braking. It is natural that frictional braking should be stronger when the halo is more dominant. In our standard model (Fig. 4), and in the more dominant disc case (Fig. 8), the large late-time differences arise because strong friction kicks in in some cases but not in all. We argue in Section 5.5 that the reason for these differences is the existence of adverse gradients in the halo DF, which can inhibit friction (Sellwood & Debattista 2006). Whatever the cause, it is clear from these two sets of runs that onset of friction and steady bar growth at late times depends on comparatively minor differences in the earlier evolution caused by the different random seeds.

In order to quantify the scatter, we compute the bi-weight estimate (Beers *et al.* 1990) of the mean and dis-



**Figure 7.** Evolution of a set of models with a more dominant halo than those shown in Fig. 4. The initial rotation curve is shown in the upper panel of Fig. 6.

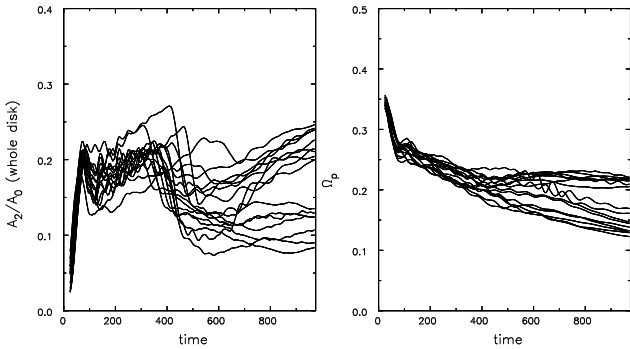


**Figure 8.** Evolution of a set of models with a less dominant halo than those shown in Fig. 4. The initial rotation curve is shown in the lower panel of Fig. 6.

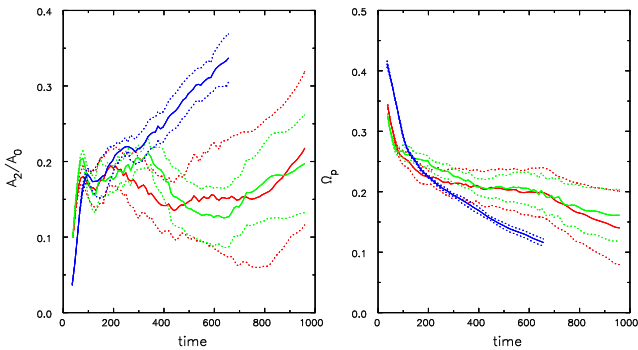


**Figure 9.** Comparison of the estimated means (solid lines) and  $\pm 1\sigma$  scatter (dotted curves) in the three different haloes shown in Figs. 4 (red), 7 (blue), & 8 (green).

person of the measurements throughout all sets of experiments.<sup>1</sup> Since bar growth is shifted slightly in time in the different runs shown in Figs. 4, 7, and 8, we apply a small time offset to the evolution of both quantities in order to ensure that the evolution coincides as the relative bar amplitude grows through 0.1, before computing the mean and

<sup>1</sup> Their algorithm assumes the data to be unimodal with a few outliers, which is manifestly not the case in our data at late times.

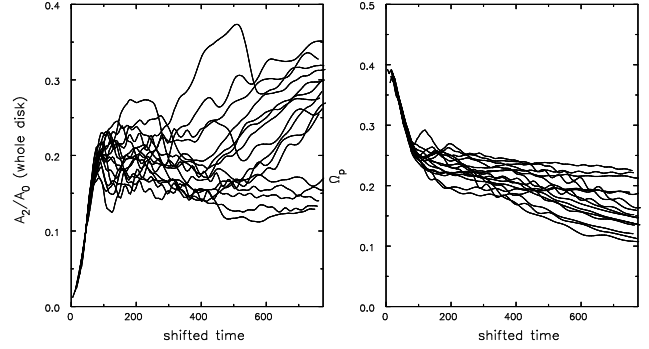


**Figure 10.** Evolution of a set of 16 runs of our standard model that used a more careful disc set up procedure.

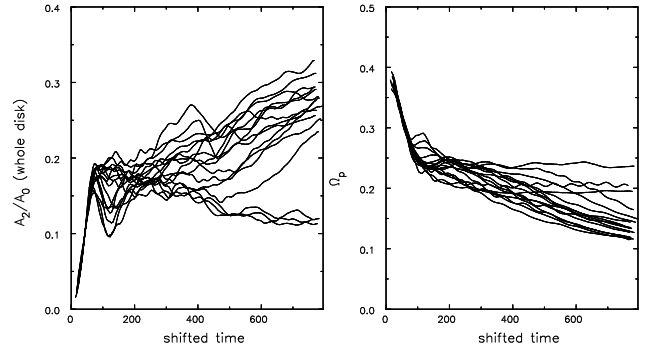


**Figure 11.** Evolution of a set of 16 runs that used Hernquist's Jeans equation procedure to set up an approximate equilibrium for the halo particles. The bar amplitude grows at late times and the pattern decreases in all but three of these cases.

scatter from each set. Fig. 9 shows the time evolution of the means and scatter of the bar amplitude and pattern speed for all three haloes. It is clear that the stochastic spread is greatest for our standard halo (red lines), less for the less dominant halo (green lines) and least for the more dominant halo (blue lines).

## 4.2 Particle selection

Fig. 10 shows the consequence of selecting disc particles in a deterministic manner from an approximate DF as described in Sections 2.2 & 3.1. This procedure still has a random element when choosing the precise values of  $E$  &  $L_z$  within each sub-area, and the simulations have noisy starts because we randomly select the radial and azimuthal phases of the particles. The 16 different runs used different random seeds and are to be compared with those shown in Fig 4, for which disc particle velocities were selected from Gaussians whose widths were estimated from the Jeans equations in the epicycle approximation. There is no significant improvement, and in this case 6/16 runs have not slowed much by  $t = 800$ .

The consequences of selecting *halo* particle velocities from Gaussians whose widths are determined from the Jeans equations (Hernquist 1993), are shown in Fig. 11. With this more approximate halo equilibrium we see that all but 3/16 bars grow and slow. The non-slowing fraction was 5/16 in a similar set of experiments (not shown) in which the halo

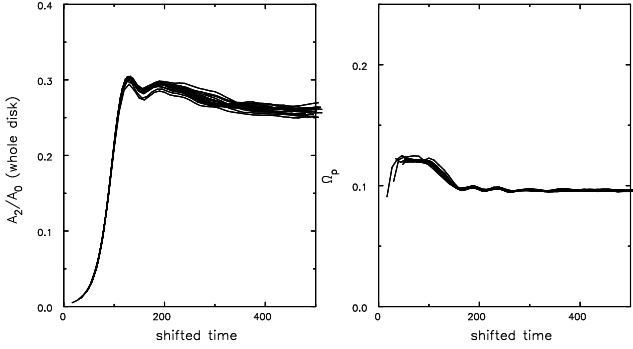


**Figure 12.** Evolution of the bar starting from 16 different selections of particles from the same DF of the isochrone/5 disc.

**Table 2.** Numerical parameters for our 2D simulations

	Isochrone	Standard model
Grid ( $N_R, N_\phi$ )	(180,256)	(170,256)
Sectoral harmonics	$0 \leq m \leq 8$	$0 \leq m \leq 8$
Outer radius	$3.995a$	$6.23R_d$
Softening rule	Plummer	Plummer
Softening length $\epsilon$	$0.05a$	$0.1R_d$
Number of particles	500 000	various
Equal masses	yes	yes
Shortest time step	0.025	0.0125
Time step zones	1	3

particles were selected from the DF by the accept/reject method, instead of deterministically for Fig. 4.

Thus we find a weak trend in these results with the quality of the different halo set-up procedures. The fraction of bars that do not experience strong friction rises to almost half when we use the most careful set-up procedure we have been able to devise for the halo, whereas use of the density profile to choose radii and Jeans equations to set halo velocities results in a large majority (13/16) of bars that experience strong friction (Fig. 11). This trend is also consistent with the weak dependence on halo particle number reported in Appendix B, where we find that the larger the halo particle number, the smaller the fraction of bars that slow. We also find a larger fraction of slowing bars when we use equal mass particles. These results hint that still larger calculations that are set up with extreme care may evolve in a consistent manner independent of the random seed, but we have been unable to demonstrate this.

## 5 SOURCES OF STOCHASTICITY

In this section, we describe and illustrate five sources of stochasticity, four of which contribute to the large scatter just described.

### 5.1 A Reproducible Result

We start from a simple unstable disc model for which the outcomes of simulations do not diverge with different random selections of initial particles. Fig. 12 shows results from noisy start simulations in 2D of an isochrone/5 disc, in which

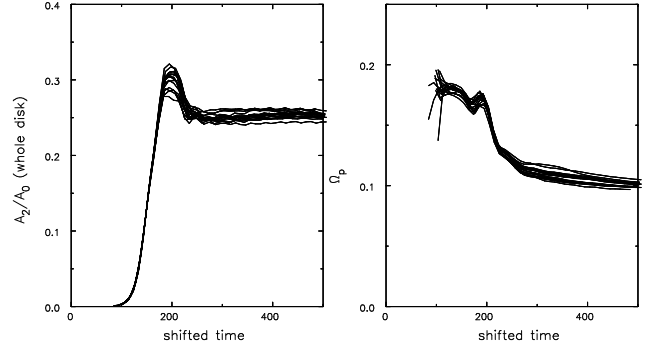


**Figure 13.** The time evolution of the bar amplitude and pattern speed in a quiet start isochrone/8 disc in which  $Q \simeq 1.2$ . Note the somewhat larger spread compared with that shown in Fig. 12.

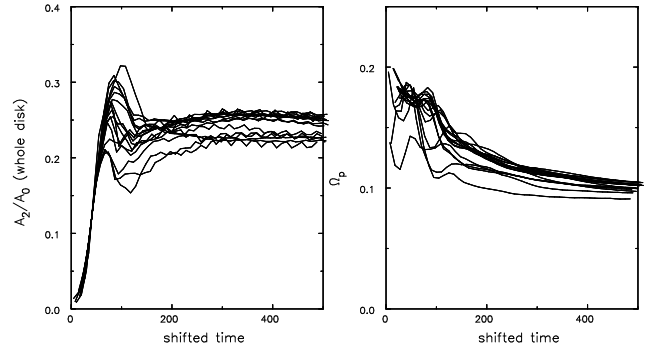


**Figure 14.** Evolution of the bar in a noisy start isochrone/8 disc in which particles are drawn from the same DF as was used for Fig. 13.

$Q \simeq 1.6$ ; numerical parameters are given in Table 2. The different curves come from separate simulations with different selections of particles from the *same* DF, using the “deterministic” procedure described in Section 2. The small scatter in the bar amplitude at late times can be further reduced by restricting disturbance forces to the  $m = 2$  sectoral harmonic only.

### 5.2 Multiple Modes

Most unstable disc models support a large set of small-amplitude, unstable modes having a wide range of growth rates (*e.g.* Toomre 1981; Jalali 2007). These linear modes, even those with the same angular periodicity, grow independently for as long as all disturbance amplitudes remain small. If the seed amplitudes of all modes are low, the first to saturate will be the most rapidly growing. In most unstable discs, the fastest growing mode is generally the simplest, or fundamental, mode that is usually dubbed the bar mode. But if the growth rate of the bar mode does not exceed that of the next most vigorous mode by a large enough margin for some seed amplitudes, then both may have comparable amplitude when one saturates. The consequence of two or more modes reaching large amplitude at similar times but with random phases can lead to constructive or destructive interference in the measured amplitudes as the “bar”



saturates. Non-linear effects then cause such differences to persist.

We use the slightly cooler  $m_K = 8$  isochrone disc to demonstrate this behaviour explicitly and, to avoid additional complications, we restrict disturbance forces to those arising from the  $m = 2$  sectoral harmonic only. Figs. 13 & 14 illustrate the dependence of the outcome on the initial noise amplitude. The quiet start simulations in Fig. 13 are good enough that the growth rates of the two most rapidly growing  $m = 2$  modes can be estimated by fitting to data from the extensive period of evolution before growth ends (e.g. Sellwood & Athanassoula 1986). We find the growth rate of the second mode to be some 85% of that of the bar mode and that its amplitude (peak  $\delta\Sigma/\Sigma$ ) can be within a factor of a few of the dominant mode as the bar saturates. The consequence is a slight increase in the scatter of the later bar amplitudes in this case compared with the case for the hotter disc shown in Fig. 12.

The mild scatter in Fig. 13 requires a quiet start, which decreases the seed amplitude of all non-axisymmetric disturbances that grow for  $\sim 100$  time units before the rising amplitudes even become discernible in the figure. The much larger seed amplitudes when noisy starts are used do not allow the dominant mode to outgrow all others before saturation, with the consequences illustrated in Fig. 14. The same sets of particles were used as for the results shown in Fig. 13, but we placed the image particles at random azimuths, instead of evenly. The period of rising amplitude is too short to allow more than very rough measurements of the growing modes, but it is clear that multiple unstable modes having comparable growth rates are seeded at large initial amplitudes by the shot noise. With such high seed amplitudes, there is not enough time for the most rapidly growing mode to outgrow the others, which therefore leads to very substantial variations in the final bar amplitudes. Note that this did not happen in the warmer disc (Fig. 12), which also used a noisy start, since in that case all growth rates are lower, while the growth rate of the dominant bar mode exceeds that of all others by a larger margin.

Notice also that not only is there greater scatter in both the bar amplitude and pattern speed in Fig. 14, but both quantities scatter to lower values. We find indications that runs having lower pattern speed have the more dominant second mode. The fundamental bar mode, when it has time to outgrow the second mode, peaks at a greater amplitude and then relaxes back to lower value, as always happens in Fig. 13. But when the second mode is competitive, the bar amplitude generally has a lower initial peak, and may even rise subsequently.

### 5.3 Swing-amplified noise

Our standard model is more complicated than the isolated isochrone disc. In particular, the inner rotation curve (Fig. 1) rises steeply where the halo density cusp dominates. Recall that a mode is a standing wave oscillation of the system, which can be neutral, growing, or decaying. The dominant linear global modes, known as cavity modes, in bar unstable discs are standing waves between the centre and corotation that must have a high enough pattern speed to avoid any inner Lindblad resonances (Toomre 1981; Binney & Tremaine 2008, pp. 508-518). The consequence of a steeply rising rota-

tion curve is to make the maximum of the function  $\Omega - \kappa/2$  rise to high values near the centre, requiring any linear bisymmetric modes to have very high pattern speeds, small corotation radii, and to have very low growth rates (because the inner disc is not all that responsive).

The outer disc, on the other hand, is highly responsive but has no cavity-type modes. We see evidence for weak edge-type modes, which arise from a steep density gradient (Toomre 1981) at the sharply truncated outer edge, but they are sufficiently far out and of low enough frequency to be decoupled from the bar forming process in the inner disc.

Shot noise from the particles is vigorously amplified, but transient swing-amplified responses should be damped at the inner Lindblad resonance (ILR) of the disturbance (Toomre 1981; Binney & Tremaine 2008, p. 510), as long as the amplitude remains tiny. Large amplitude waves are not damped, however, and trap disc particles near the ILR into a bar-like feature (Sellwood 1989).

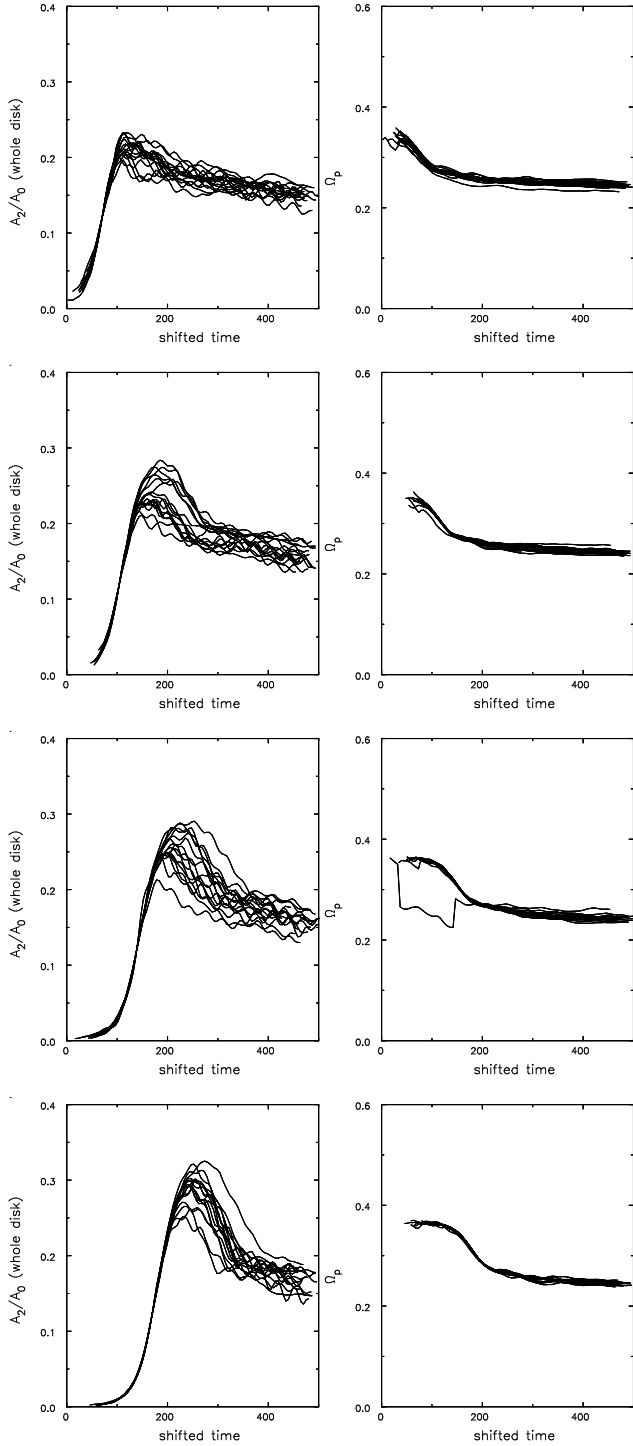
Bar formation through amplified noise inevitably leads to a range of bar properties, but it is fortunate that the range turns out to be surprisingly narrow. To illustrate this, we study bar formation in our standard model in simplified simulations in which the motions of disc particles are confined to a plane, and the halo particles are replaced by a rigid mass component that simply provides the extra central attraction to yield the same rotation curve as shown in Fig. 1. This approach has several advantages: the calculations are less expensive in computer time, but more importantly the dynamics is simpler because both bar buckling and halo friction are eliminated, enabling us to isolate the bar formation process from these other complicating aspects of the overall evolution.

Fig. 15 shows 4 sets of 16 runs each in which  $N$  is increased by a factor 10 from row to row, from  $N = 50K$  at the top, to  $N = 50M$  for the bottom row. The results from each run have been slightly shifted horizontally so that the amplitude passes through 0.1 at the same time (the mean for the 16 runs) as described above. The bar amplitude has a higher peak than in Figs. 4 & 5 in part, at least, because we use a different softening rule in 2D. The discrepant line in one of the pattern speed panels shows that the bar cannot always be identified in the early stages, but eventually it is in all cases.

Fig. 16 shows the evolution of the means and scatter in the four sets of experiments, and reveals that the main effects of increasing  $N$  are threefold: the formation of the bar is delayed because of lower seed noise, the mean peak bar amplitude increases and the scatter in the amplitude evolution *rises* with increasing particle number, at least to  $N = 5M$ . The pattern speeds are better behaved, with scatter decreasing as  $N$  rises.

Because these calculations have less freedom, the amplitude variation is much less than those shown in Fig. 4, which have the same numbers of disc particles as those in the second row of Fig. 15. Nevertheless, the spread in the bar amplitudes after the initial rise remains quite high. The pattern speed does not decline as much because the rigid halo does not cause dynamical friction.

Since amplified noise is intrinsically stochastic, the dominant transient responses in different random realizations of the disc must differ. The possible frequency range of the dominant pattern is broad, but not unbounded; the rota-



**Figure 15.** Evolution of the bar in four sets of 16 runs with different random seeds for the disc particle coordinates. The number of particles rises by a factor of 10 from row to row, ranging from 50K in the top row to 50M in the bottom row.

tion curve and surface density profile, among other properties, cause the responsiveness of the disc to vary with radius, and therefore the dominant responses have corotation radii in the region where the disc is most responsive. Thus the very first collective responses at low, but fixed,  $N$  lead to initial bars having a range of strengths, *i.e.* sizes, with the

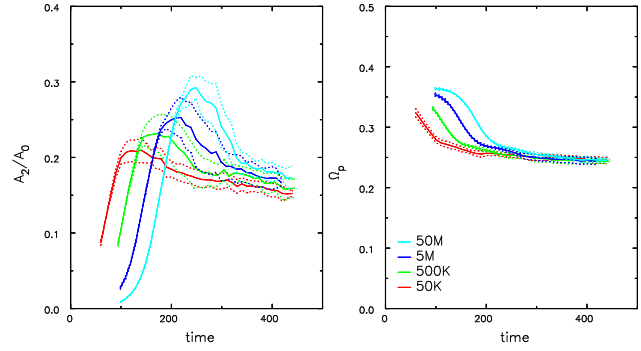


**Figure 16.** Summary plot showing the means and  $\pm 1\sigma$  scatter of the runs shown in Fig. 15.

larger bars developing more slowly because the clock runs more slowly farther out in the disc. (The time delays have been removed from Fig. 15.)

The larger the number of particles, the longer it takes for the bar to form (Fig. 16). Initial transient responses occur at roughly the same rate but, in experiments with larger  $N$ , the lower initial amplitudes do not lead to immediate bar formation. Subsequent amplification events tend to be of greater amplitude, and to occur farther out in the disc. Thus we see that a lower level of shot noise favours large amplitude responses farther out in the disc that briefly lead to longer and stronger bars.

The pleasant surprise is that after the initial transient episodes produce bars of different sizes and angular speeds, we observe (Fig. 16) that subsequent evolution causes the range of bar strengths to narrow. Also most of the systematic trends with particle number are erased in the subsequent evolution, and neither the bar amplitude nor its pattern speed at later times exhibits more than a mild dependence on  $N$ . It is fortunate that a degree of uniformity of the bar properties emerges after such tumultuously different evolution. But it is far from obvious why it should, especially since the model could have supported bars of wide range of sizes (*e.g.* Fig. 4).

The results shown in Fig. 15 are for models with rigid haloes in which the disc was created using the Jeans equations (Section 2.2). Far from becoming better behaved, the scatter in the amplitude evolution *increases* as  $N$  rises! We conducted a similar set of tests, also with rigid haloes, for which disc particles were selected deterministically from an approximate DF. The evolution of these more carefully set up models resulted in slightly improved behaviour: the bar formed somewhat more slowly, peaked at a little lower amplitude for the same value of  $N$ , and the scatter no longer varied systematically with  $N$ . However, the final bar amplitude and pattern speeds were within the ranges shown in Fig. 15.

Unlike the results for the isochrone presented in Appendix C, the more careful selection of particles yielded only a slight reduction in the spread in evolution. It is likely that this difference in behaviour of the two discs is due to the difference in bar forming mechanism; the instability of the isochrone disc is due to strongly unstable linear global modes, whereas as the bars in our standard model form through non-linear trapping of swing-amplified parti-

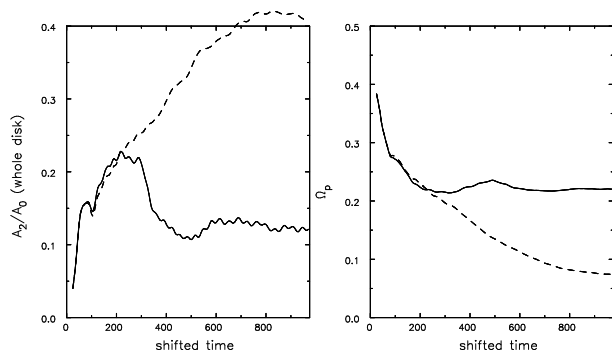


**Figure 17.** Comparison of the time evolution of two runs that differ only in the imposition of reflection symmetry about the midplane. The solid curves are for a model taken from Fig. 4 in which vertical forces are unrestricted while the dashed curves show the evolution of the same initial model when vertical forces from the disc are constrained to be symmetric about the midplane.

cle noise that would be less affected by the quality of the equilibrium.

Thus far we have discussed only bisymmetric instabilities, but other low-order instabilities may also be competitive. In fact, we find some evidence for lop-sidedness, which we describe in the next subsection.

#### 5.4 Bending modes

The bars in most 3D simulations suffer from buckling instabilities that, when they saturate, thicken the bar in the vertical direction (*e.g.* Combes & Sanders 1981; Raha *et al.* 1991). In many, but not all, cases the evolution of this bending mode is quite violent and weakens the bar significantly, while the central density of the bar rises, as reported by Raha *et al.* The radial rearrangement of mass evidently liberates the energy needed to puff up the bar in the vertical direction.

The time of saturation of the buckling mode depends on a variety of factors, such as the formation time of the bar, and the initial seed amplitude of the bending mode, the strength of the bar, *etc.* Several of these factors will in turn depend on the already stochastic formation of the bar. It is hardly surprising therefore, that this event occurs over a wide range of times and with a wide range of severity (Fig. 4), thereby compounding the overall level of stochasticity.

The buckling mode can be inhibited by artificially imposing reflection symmetry about the mid-plane, which causes a substantial change to the evolution. Fig. 17 compares the evolution for one case; the dashed curves show that when buckling is inhibited, the bar continues to grow in amplitude, while slowing, for a long period. On the other hand, the amplitude drops quite abruptly when the bar buckles (solid curves) and the subsequent amplitude and pattern speed hold approximately steady.

Not all the bars in the runs illustrated in Fig. 4 experience a violent buckling event. In some cases the bar amplitude does not decrease after the initial peak, while in others the amplitude drop is more gradual.

Fig. 18 shows the effect of suppressing the  $m = 1$  sec-

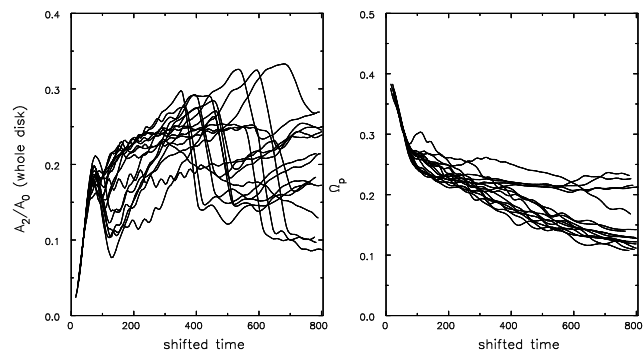


**Figure 18.** Evolution of a set of 16 runs that differ from those shown in Fig. 4 only in the suppression of lop-sidedness about the  $z$ -axis.

toral harmonic about the  $z$ -axis for both the disc and halo particles. This has the effect of preventing the centres of either component from leaving the  $z$ -axis. (Suppressing the  $l = 1$  component of the halo force calculation would nail the centre of that component to the origin, which would prevent the halo from responding properly to a buckling mode.) With lop-sidedness inhibited in this way, all bars buckle, and all but one do so violently with a large decrease in amplitude. This difference in buckling behaviour from that shown for the same initial models in Fig. 4 indicates that buckling is strongly influenced by mild lop-sidedness, which has not been reported elsewhere, as far as we are aware. We could not find any evidence for lop-sided instabilities in the runs shown in Fig. 4, and the distance between the centroids of the halo and disc particles was  $\lesssim 0.002R_d$ . As it seems unlikely that such small offsets could have such a large effect on the saturation of the buckling mode, we think it possible that an anti-symmetric mode competes. Investigation of this possibility here would be too great a digression.

Despite the violence of most buckling events, most bars in these restricted simulations continue to slow after the buckling event and amplitude growth resumes. The four exceptions are bars that remained strong right after their formation and did not slow much either before or after the buckling event.

Results reported in Appendix B show that the buckling behaviour is also somewhat sensitive to particle softening.

Klypin *et al.* (2008) report that the violence of the buckling event also depends on the initial thickness of the disc. This is as expected, since Merritt & Sellwood (1994) showed that buckling is a consequence of a collective instability that arises in systems in which the velocity distribution becomes too anisotropic, and thickening the disc reduces the flattening of the velocity ellipsoid. However, in a separate test with a set of runs with twice the disc thickness (not shown), we still find a similar degree of scatter in the late evolution.

#### 5.5 Incidence of Dynamical Friction

Fig. 19 shows that the divergent late-time evolution of the runs shown in Fig. 4 is due to differences in the incidence of dynamical friction. The lines are coloured blue when the torque acting on the halo  $dL_z/dt < 5 \times 10^{-5} GM^2/R_d$ , and are red otherwise.

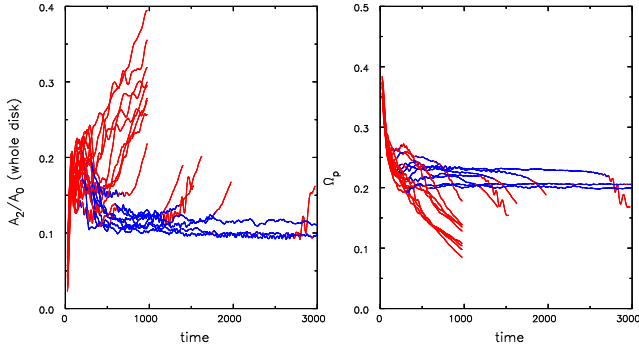


**Figure 19.** The results shown in Fig. 4, but with the curves colored blue when the torque on the halo is low and red otherwise. The calculations were continued for models that had not slowed by  $t = 1000$  and were stopped either at  $t = 3000$  or soon after friction kicked in, which happened in all but two cases.

The absence of bar friction may have a variety of causes: (a) low halo density, (b) a weak bar, and (c) metastability caused by local adverse gradients in the density of halo particles as function of angular momentum (Sellwood & Debattista 2006). The halo density is just about the same in all cases, but the bar strength varies widely and it is clear that the weaker bars experience little friction.

The third possibility is indicated by the evidence in Fig. 19, since friction eventually resumes, sometimes after a very long period during which the bar amplitude does not increase; the metastable state does not last indefinitely. We argue (Sellwood & Debattista 2006) that the metastable state has a finite lifetime because weak friction at minor resonances gradually slows the bar until the more important resonances move out of the region of adverse gradients, allowing strong friction to resume.

Metastability could be caused by the buckling event, since bars that are weakened substantially by a buckling event, such as the case picked out in Fig. 17, generally do not experience much friction at late times, and their amplitudes stay low. The upward rise in the bar pattern speed at the time of buckling is shown clearly by the solid curve in Fig. 17, which we (Sellwood & Debattista 2006) found to be a likely cause of metastability. It is reasonable that the concentration of mass to the centre as the bar buckles should cause an upward fluctuation in the bar pattern speed (because the orbit periods must vary inversely as the square root of the mean interior density). However, buckling does not always lead to a cessation of friction; for example, many of the bars in the 16 runs with a more dense halo (Fig. 7) clearly buckled, but friction continued in all cases.

### 5.6 True chaos

Here we show that Miller’s (1964) instability can lead to macroscopic differences in discs. Where initial evolution is largely determined by swing-amplification of the spectrum of particle noise laid down by the random coordinates of particles, models that differ by tiny amounts quickly diverge because the subsequent spiral events depend on the details of evolution of previous events. This phenomenon causes the

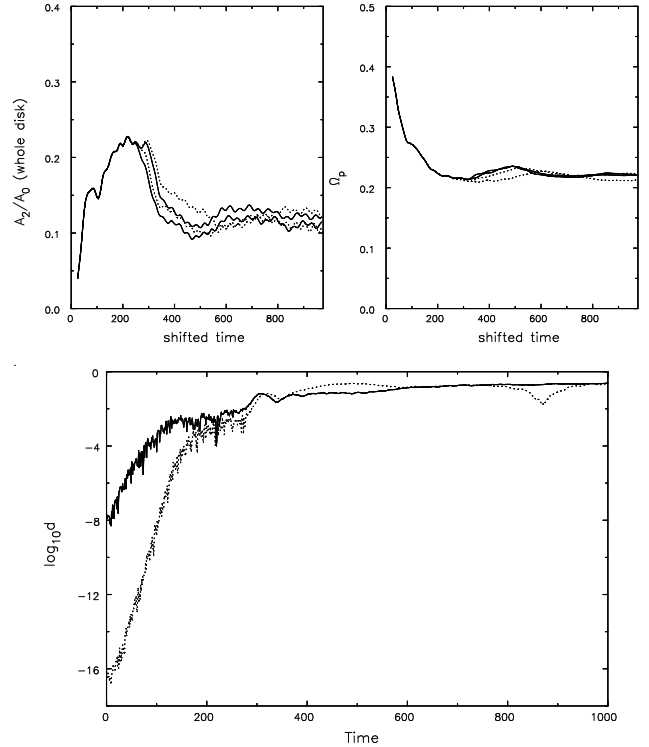


**Figure 21.** The upper panels compare the evolution of four cases that started from the identical file of particle coordinates, with all numerical parameters held fixed, except that solid lines are for calculations in single precision, dotted lines are for the identical calculations in double precision. As for Fig. 20, the order of the particles was reversed in one of each pair. The lower panel shows the time evolution of the quantity  $d$  defined in eq. (5) for both pairs of runs.

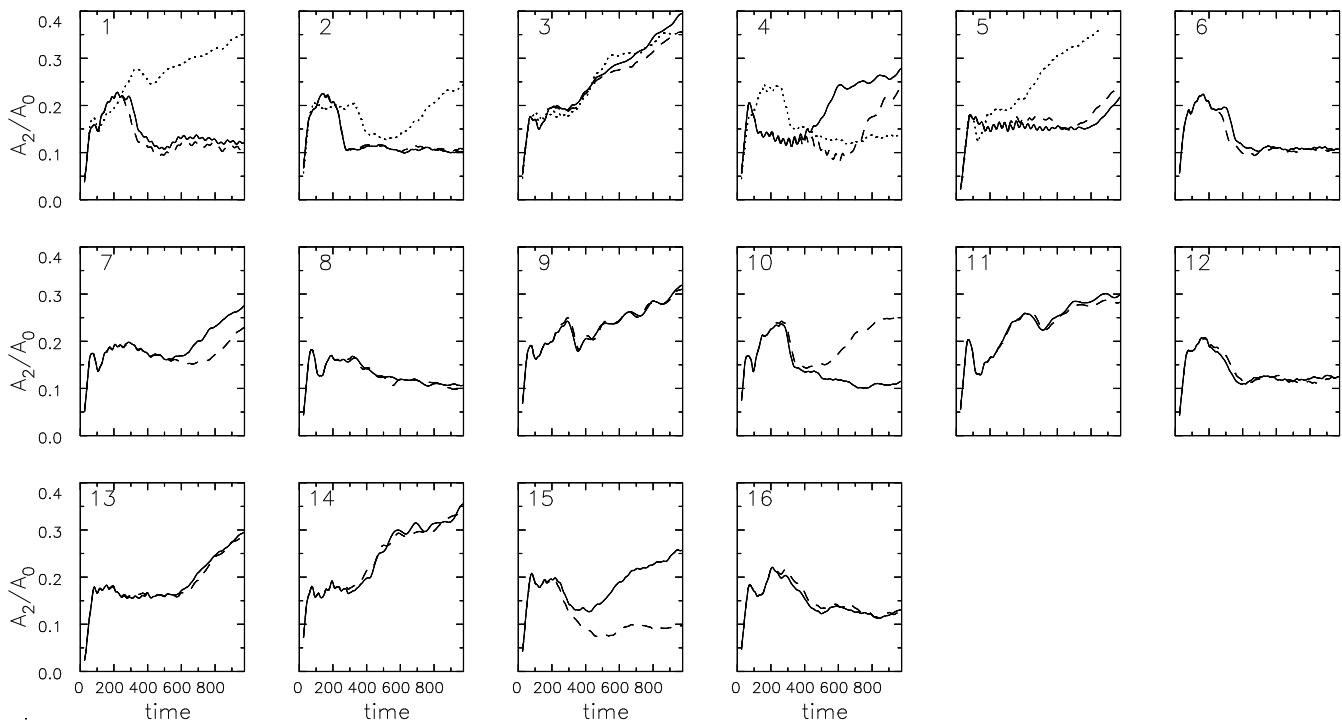
micro-chaos in  $N$ -body systems to lead to macroscopic differences in discs.

Fig. 20 compares the amplitude evolution of each case shown in Fig. 4 (solid lines) with another run of the same case with the order of the particles reversed (dashed). Thus the initial phase space coordinates of all particles were identical and are evolved with the same code on identical processors. Each pair of simulations differ only in the order in which arithmetic operations are performed, which changes the initial accelerations at the round off error level only, yet the amplitudes at late times generally differ visibly, and in some cases, *e.g.* 10 & 15, the evolution differs qualitatively.

So far, every calculation with grid codes that we have reported here was conducted using single precision arithmetic for most operations. We have checked that increased precision has no effect on the range of behaviour shown in Fig. 4, and results differ only slightly, as we now show for one case.

Fig. 21 shows that the system remains chaotic when we repeat the calculations using double precision arithmetic (dotted lines). The higher precision calculations begin to diverge visibly at about the same times as in the single precision cases, and the subsequent differences are comparable. In order to monitor the divergence in these cases, we compute the value over time of the difference

$$d = [\Re(A_{2,a} - A_{2,b})^2 + \Im(A_{2,a} - A_{2,b})^2]^{1/2} \quad (5)$$



**Figure 20.** Comparison of the amplitude evolution of the models shown in Fig. 4 (solid lines) with the same sets of particles processed in reverse order (dashed lines). The evolution of these two sets of identical runs is measurably different in all cases, and qualitatively different in some, especially cases 10 & 15. The dotted lines in the first 5 panels show the evolutions using PKDGRAV for the same files of initial particles.

between the bar coefficients (eq. A3) in these pairs of experiments ( $a$  &  $b$ ) in which the order of the particles was reversed. The solid (dotted) line in the lower panel of Fig. 21 shows the result for the single (double) precision pair. By  $t \sim 300$  the models differ quite visibly in the amplitude and phase of the bar, which accounts for the fact that  $d$  asymptotes to a lasting value where the phases of the two bars differ.

The difference,  $d$ , in double precision grows quasi-exponentially over time at first, which is symptomatic of chaos, with a Lyapunov ( $e$ -folding) time of  $\sim 4.75$  dynamical times, *i.e.*, less than 25% of the orbit period ( $\sim 20$  dynamical times) at  $R = 2.5R_d$ . Using this estimate of the Lyapunov time, the difference in the double precision case should equal the initial difference in the single precision case after  $\approx 93$  dynamical times, and the early evolution of  $d$  in the lower precision case is roughly similar to that in the double precision case with a time offset of this magnitude. Even though there is a much smaller initial difference between the two double-precision models, the seed amplitude of the instabilities is set by the shot noise, which is the same in all 4 runs. Thus the non-axisymmetric structures are almost fully developed in the double precision models by the time the dotted curve reaches the level of the start of the solid line; therefore one cannot expect the curves to overlay perfectly.

It is curious that the difference in the double precision case “catches up” with that in the single precision case. The shoulder in  $\log_{10} d$  that appears in both precisions at about  $t = 300$  seems to be responsible for this convergence, which occurs both at such a large value of  $d$  as to be well past where

exponential divergence could be expected to hold, and at a time when the bar in all four runs is fully developed.

A perfect collisionless particle system should be exactly time reversible; that is, if the velocities of all the particles were reversed at some instant, the system should retrace its evolution. Fig. 22 shows that reversed simulations do retrace their evolution for a short while, between 60 and 80 dynamical times, after which the evolution of the reversed model visibly departs from the corresponding reflection of the forward evolution. This period of successful reversibility is consistent with our Lyapunov divergence estimate: 15 Lyapunov times ( $= 71.25$  dynamical times) corresponds to a divergence of  $\sim 10^{6.5}$ , which is sufficient to alter almost every significant digit in these single precision calculations and lead to reversed evolution that becomes largely independent of that in the forward direction. Further analysis of these simulations revealed that the first signs of irreversibility appeared as differences in the leading spiral Fourier components, suggesting that vigorous swing-amplification of particle noise is primarily responsible for the short Lyapunov time.

We conclude from these tests that the  $N$ -body system we are trying to simulate is indeed chaotic. Further, the effects of chaos are not significantly worsened by round-off error in single precision; we have also verified that the full divergence of the results in Fig. 4 persists in double precision. In fact, the first author has frequently checked, and always confirmed, that no advantage results from use of higher precision arithmetic when computing the evolution of collisionless  $N$ -body systems. This conclusion is in sharp contrast with the requirements for collisional systems (*e.g.* Aarseth 2008).

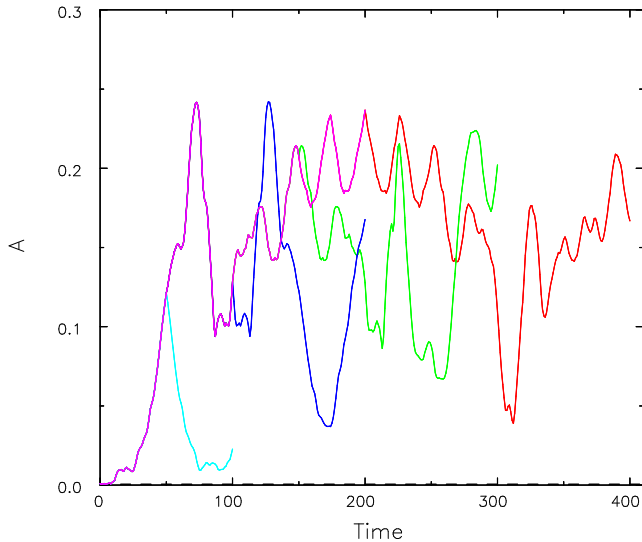


**Figure 22.** The magenta line shows the unsmoothed bar amplitude evolution of one model run to  $t = 200$ . The other lines show the continued evolution of the same model with the velocities of all the particles reversed at  $t = 50$  (cyan),  $t = 100$  (blue),  $t = 150$  (green), and  $t = 200$  (red). In all four cases, the evolution immediately after the reversal faithfully retraces the forward evolution for a period less than 100 time units. After this time the evolution departs noticeably from a reflection of the line about the reversed moment.

In none of the simulations with grid codes reported in this paper did we distribute the computation over multiple parallel processors, even though the code has been well optimized for parallel use. We adopted this strategy in order to avoid the additional randomness that is inevitable when results from multiple processors are combined in an unpredictable order.

The dotted curves in the first five panels of Fig. 20 show the result using the tree code PKDGRAV for the same initial coordinates in each case, which are reproduced from Fig. 5. Although the ranges and distributions of measured bar properties shown in Figs. 4 & 5 are similar, the results do not compare in detail, as noted above. Results from the two different codes diverge strongly in all but one case, reinforcing the conclusion of intrinsic stochasticity. Which of the two possible evolutionary paths is taken in the evolution is affected no more, and no less, by code differences than by choices of the random seed.

## 6 DISCUSSION

### 6.1 Is there a right result?

One of the most troubling aspects of the diverging evolution in Figs. 4 & 5 is that one cannot decide which of the two patterns of behaviour is “correct,” or indeed whether there could be a unique evolutionary path with a perfect code and infinite numbers of particles.

Since these models have high density centres (Fig. 1), linear stability analysis would most likely reveal that all global modes, with the possible exception of edge modes (Toomre 1981), have very low growth rates, and therefore the disc ought to be stable and not form a bar. If this is

indeed what linear theory would predict, then the “right result” with a perfect code and infinite numbers of particles would be a stable model that does not form a bar. This outcome never occurred in the  $> 400$  simulations we report here, even in cases with one hundred times our standard number of disc particles (Fig. 15).

The level of shot noise in a simulation with  $\gtrsim 1$  million particles is clearly  $\sim 100$  times higher than would be present in a real galaxy if the  $\sim 10^{10}$  stars were randomly distributed. But the mass in real galaxy discs is clumpier because of the existence of star clusters and giant gas clouds, which raises the amplitude of random potential fluctuations – although the density fluctuation spectrum may not be the same as that of shot noise in the simulations. Nevertheless, it seems most unlikely that a real galaxy closely resembling the model used in our simulations could avoid being barred.

### 6.2 Dynamical Friction

The greatest source of divergence is the bimodal nature of dynamical friction, which is avoided for a long time in some cases, but kicks in immediately in others, causing the bar to slow and increase in strength by a substantial factor. It is likely that friction is avoided because the needed gradient in the halo DF as a function of angular momentum has been flattened by the earlier evolution of the model, as reported by Sellwood & Debattista (2006). The fact that this happens here more frequently than we found with the model created by Valenzuela & Klypin (2003) may have two causes: their model had both a less dominant disc and an initial halo with significant departures from equilibrium.

In Section 4.2, we reported a weak trend towards a larger fraction of non-slowng bars as we took greater care over the initial selection of particles; further, the largest fraction (10/16) occurs in the test with four times the number of halo particles reported in Appendix B. This weak trend suggests that the metastable state is reached more readily as the quality of the simulation is improved.

However, Sellwood & Debattista (2006) found that the metastable state, in which the bar did not slow, was not indefinite and friction eventually resumed, as we also find here (Fig. 19). Furthermore, they found the metastable state to be fragile, and friction would resume soon after a tiny perturbation, such as the distant passage of a small satellite galaxy. Thus, even though the metastable state is reached more frequently in higher quality calculations, it is unlikely it could be sustained in real galaxies. We conclude therefore that the strongly braked and growing bar is the most “realistic” outcome from these simulations.

### 6.3 Introducing a seed disturbance

Holley-Bockelmann *et al.* (2005) attempted to make the outcome more predictable by seeding the bar instability by an externally applied transient squeeze. We argue here that this approach is not the panacea it may seem.

In the case of discs having well-defined global instabilities, noisy starts already seed the dominant unstable modes at high amplitude (Section 5.2; Sellwood 1983). If a seed disturbance is to prevail, it must be imposed at such high amplitude as to be practically non-linear at the outset. Furthermore, the objective must be to favour the dominant mode

over the others, which cannot be achieved by a simple perturbation. Instead, one must impose both the detailed radial shape and perturbed velocities of the mode, which are generally not known. A more generic disturbance, such as a “squeeze” will simply raise the amplitude of all the modes and transients, giving *less* time for the dominant mode to outgrow the others. Quiet starts (Section 2.3; Sellwood 1983; Sellwood & Athanassoula 1986), however, have the effect of reducing the initial amplitudes of all non-axisymmetric disturbances to such an extent that there is ample time for the most rapidly growing mode to prevail. Thus the outcome of a quiet start experiment is tolerably reproducible without the need to apply an additional seed (Fig. 13).

The situation is far more difficult in the case, as in the present study, where the disc has no prevailing global instabilities, since the evolution of a simulation is dominated by swing-amplified shot noise. Quiet starts are all but useless in these circumstances also, since they break up rapidly as the tiny seed noise is swing amplified, with similar outcomes, only slightly delayed, to those from noisy starts. Cranking up the particle number does not reduce variations in the bar amplitude at later times (they actually increased in Fig. 15), but does delay bar formation. Because of this, perhaps a suitable seed disturbance in a very large  $N$  disc may prevail over the amplified shot noise and lead to a more reproducible outcome. We have not explored this idea here and leave it for a future study.

## 7 CONCLUSIONS

We have shown that simulations over a fixed evolutionary period of a simple disc-halo galaxy model can vary widely between cases that differ only in the random seed used to generate the particles, even though they are drawn from identical distributions. Fig. 4 shows that the late-time amplitude of the bar can differ by a factor of three or more while the stronger bars may have half the pattern speed of the weaker ones. Fig. 19 shows that the largest differences are only temporary, however. We have deliberately focused our study on a case which displays this extreme bad behaviour. Stochastic variations are inevitable, but evolution is generally less divergent; *e.g.*, when the halo has both higher and lower density (*e.g.* Fig. 9).

We have shown that the divergent outcomes do not result from a numerical artefact, since they are independent of numerical parameters (Appendix B). Also, similar behaviour occurs with a code of a totally different type (PKDGRAV, see Fig. 5). Instead, this extreme stochasticity results from a number of physical causes that we have identified and illustrated. The most important for our model are: swing-amplified particle noise, the variations in the incidence and severity of buckling, and the incidence of dynamical friction. We have separately shown (Fig. 14) that other disc models having a well-defined spectrum of global modes can have a range of outcomes because of the coexistence of competing instabilities.

The calculations in Fig. 4 are of models that were set up with considerable care so as to be as close as possible to equilibrium. An additional level of unpredictability can result from less careful set-up procedures, as illustrated in Appendix C.

We have been aware for many years that simulations including disc components can be reproduced exactly only if the arithmetic operations are performed in the same order to the same precision, and that differences at the round-off error level can lead to visibly different evolution. However, we have been surprised by the strongly divergent behaviour of the particular model studied here. The pairs of divergent results in Fig. 20 are the stellar dynamical equivalents of the possible macroscopic atmospheric consequences of Lorenz’s butterfly flapping its wings. Because the system is chaotic, improved precision arithmetic is of no help in reducing the scatter in the outcomes.

The divergence in different realizations of our standard case arises from a temporary delay in the incidence of dynamical friction, which is determined by minor details of the early evolution. Strong friction causes the bar to both slow and grow; in some cases this occurs right after bar formation, but in others the bar rotates steadily at an almost constant amplitude for a protracted period. Friction is avoided when the earlier evolution causes an inflexion in the angular momentum density gradient of the halo. We (Sellwood & Debattista 2006) previously described this as a metastable state because it did not last indefinitely even when the evolution was unperturbed, and we also showed that mild perturbations could cause friction to resume. We find that the fraction of initially non-slowng bars increases as greater care is taken over the initial set up because the smaller fluctuations in such models are less likely to nudge the model out of the metastable state.

We argue in Section 6 that the most realistic outcome of these experiments is the slowing and growing bar, despite the fact that we find the delayed friction result increasingly often as we improve the quality of the initial set-up and of the simulation. Since most real galaxies are likely to be subjected to frequent mild perturbations, we conclude that slowing and growing bars are in fact the more realistic outcome.

Since the possible evolution of the simulation is not unique, multiple experiments of essentially the same model are needed in order to demonstrate that the behaviour is robust. Furthermore, the failure of an experiment by one group to reproduce the results of a similar experiment by another may not be the result of errors or artefacts in either or both codes, but rather a reflection of a fundamental stochasticity of the system under study.

Klypin *et al.* (2008) report a similar, but less extensive, comparison between two tree codes and an adaptive mesh method, and conclude that all the codes produce “nearly the same” results in simulations performed with sufficient numerical care. However, inspection of the comparatively short evolution shown in their Fig. 8 reveals slowly diverging outcomes, even between two simulations run with tree codes. They also report (their Fig. 1) a strongly divergent result when the time step was varied; the sharp decrease in bar strength in this one case was clearly a consequence of a more violent buckling event than in their comparison cases. Such a difference could have easily arisen from stochastic variations of the kind discussed here, and the conclusion that the shorter time step is required no longer follows. We show here (Appendix B), as do Dubinski *et al.* (2009), that results are robust to wide variations in time step. Clearly when stochasticity can lead to sharply divergent results, pa-

parameter tests that throw up surprises are conclusive only after ensembles of particle realizations have been simulated. This must also be a requirement for meaningful comparisons between codes or workers.

Since the principal sources of stochasticity are connected to disc dynamics, they are unrelated to the halo particle number question raised by Weinberg & Katz (2007). Not only has Sellwood (2008) already shown that friction can be captured adequately with moderate particle numbers, but we have found here that the expected bar friction arises more readily in haloes with fewer or equal mass halo particles, or in haloes that are not set up with great care – which is not the expected behaviour were particle scattering dominant. Instead, small departures from equilibrium can upset the delicate metastable state in which bars can rotate without friction (Sellwood & Debattista 2006).

It should be noted that bars that slow through dynamical friction also grow in length, as reported earlier by Athanassoula (2002). Nevertheless, for these models the ratio of corotation radius to bar semi-axis  $\mathcal{R} > 1.4$ , as expected for a moderate-density halo (Debattista & Sellwood 2000). Those bars that avoid friction for a long period, however, have  $\mathcal{R} < 1.4$ , as also found by Valenzuela & Klypin (2003), but this metastable state is fragile and unlikely to arise in real galaxies (Sellwood & Debattista 2006).

Since all  $N$ -body simulations are intrinsically chaotic, they can be reproduced exactly only if the same arithmetic operations are performed in the same order with the same precision, as noted in the introduction, and borne out in Fig. 20. These requirements dictate the use of the same code, compiler, operating system, and hardware. Further, if the calculation is stopped and then resumed, it is important to save sufficient information so that the acceleration used to advance each particle at the next step is identical, to machine precision, to that it would have been had the calculation not been interrupted. This can be arranged without too much difficulty, if the calculation is run on a single processor. However, simulations that distribute work over parallel processors in computer clusters would be exactly reproducible only if care is taken to ensure that the work is distributed and the results are combined in a fully predictable manner.

Provided the divergence is slight, exact reproducibility is of little scientific interest, although such a capability is useful to the practitioner. But when, as described here, the model under test can have strongly divergent behaviour that arises from differences that begin at the round off level with the same code on the same machine, comparison of results between different codes and on different platforms becomes much less likely to produce agreement, even when the simulations share the same file of initial coordinates. It is ironic that the model used here was in fact that selected as a test case for code comparison; fortunately, the authors discovered its unsuitability in time!

## ACKNOWLEDGMENTS

We thank Scott Tremaine, Tom Quinn, and the referee, Martin Weinberg, for helpful comments on the manuscript and Juntaí Shen for discussions. This work was supported by grants to JAS from the NSF (AST-0507323) and from NASA

(NNG05GC29G) and by a Livesey Grant from the University of Central Lancashire to VPD. The PKDGRAV simulations were performed at the Arctic Region Supercomputing Center (ARSC).

## REFERENCES

- Aarseth, S. J. 2008, in “The Cambridge N-Body Lectures”, Lecture Notes in Physics, **760** (Springer-Verlag: Berlin Heidelberg), p. 1
- Arfken, G. 1985, *Mathematical Methods for Physicists*, 3rd ed. (Orlando: Academic Press)
- Athanassoula, E. 2002, ApJL, **569**, L83
- Athanassoula, E. 2003, MNRAS, **341**, 1179
- Beers, T. C., Flynn, K. & Gebhardt, K. 1990, AJ, **100**, 32
- Binney, J. & Tremaine, S. 2008, *Galactic Dynamics* 2nd edition (Princeton: Princeton University Press) (BT08)
- Camm, G. L. 1950, MNRAS, **110**, 305
- Combes, F. & Sanders, R. H. 1981, A&A, **96**, 164
- Debattista, V. P. & Sellwood, J. A. 2000, ApJ, **543**, 704
- Dehnen, W. 2001, MNRAS, **324**, 273
- Diemand, J., Moore, B., Stadel, J. 2004, MNRAS, **353**, 624
- Dubinski, J., Berentzen, I. & Shlosman, I. 2009, ApJ, **697**, 293
- Earn, D. J. D. & Sellwood, J. A. 1995, ApJ, **451**, 533
- El-Zant, A., Hoffman, Y., Primack, J., Combes, F. & Shlosman, I. 2004, ApJL, **607**, L75
- Erickson, S. A. 1975, PhD thesis, MIT.
- Frenk, C. S., *et al.* 1999, ApJ, **525**, 554
- Hernquist, L. 1990, ApJ, **356**, 359
- Hernquist, L. 1993, ApJS, **86**, 389
- Holley-Bockelmann, K., Weinberg, M. & Katz, N. 2005, MNRAS, **363**, 991
- Jalali, M. A. 2007, ApJ, **669**, 218
- Kalnajs, A. J. 1976, ApJ, **205**, 751
- Kalnajs, A. J. 1978, in *Structure and Properties of Nearby Galaxies* IAU Symposium **77** eds. E. M. Berkhuisjen & R. Wielebinski (Dordrecht:Reidel) p. 113
- Klypin, A., Valenzuela, O., Colín, P. & Quinn, T. 2008, arXiv:0808.3422
- Kuijken, K. & Dubinski, J. 1995, MNRAS, **277**, 1341
- McGlynn, T. A. 1984, ApJ, **281**, 13
- Merritt, D. & Sellwood, J. A. 1994, ApJ, **425**, 551
- Miller, R. H. 1964, ApJ, **140**, 250
- Monaghan, J. 1992, ARAA, **30**, 543
- Monaghan, J. & Lattanzio, 1985, A&A, **149**, 135
- Power, C., Navarro, J. F., Jenkins, A., Frenk, C. S. & White, S. D. M. 2003, MNRAS, **338**, 14
- Prendergast, K. H. & Tomer, E. 1970 AJ, **75**, 674
- Raha, N., Sellwood, J. A., James, R. A. & Kahn, F. D. 1991, Nature, **352**, 411
- Romeo, A. 1992, MNRAS, **256**, 307
- Sellwood, J. A. 1981, A&A, **99**, 362
- Sellwood, J. A. 1983, J. Comp. Phys., **50**, 337
- Sellwood, J. A. 1985, MNRAS, **217**, 127
- Sellwood, J. A. 1989, MNRAS, **238**, 115
- Sellwood, J. A. 2003, ApJ, **587**, 638
- Sellwood, J. A. 2008, ApJ, **679**, 379
- Sellwood, J. A. & Athanassoula, E. 1986, MNRAS, **221**, 195
- Sellwood, J. A. & Debattista, V. P. 2006, ApJ, **639**, 868



- Sellwood, J. A. & Evans, N. W. 2001, *ApJ*, **546**, 176  
 Sellwood, J. A. & McGaugh, S. S. 2005, *ApJ*, **634**, 70  
 Sellwood, J. A. & Merritt, D. 1994, *ApJ*, **425**, 530  
 Shlosman, I. & Noguchi, M. 1993, *ApJ*, **414**, 474  
 Shu, F. H. 1969, *ApJ*, **158**, 505  
 Spitzer, L. 1942, *ApJ*, **95**, 329  
 Stadel, J. G., 2001, Ph.D. thesis, University of Washington.  
 Toomre, A. 1964, *ApJ*, **139**, 1217  
 Toomre, A. 1981, in *The Structure and Evolution of Normal Galaxies*, eds. S. M. Fall & D. Lynden-Bell (Cambridge: Cambridge University Press), p. 111  
 Valenzuela, O. & Klypin, A. 2003, *MNRAS*, **345**, 406  
 Vandervoort, P. O. 1970, *ApJ*, **161**, 87  
 Weinberg, M. D. & Katz, N. 2007, *MNRAS*, **375**, 460  
 Young, P. 1980, *ApJ*, **242**, 1232  
 Zhang, M. & Magorrian, J. 2008, *MNRAS*, **387**, 1719

## APPENDIX A: CODES AND SOFTENING RULES

### A1 Force Determination Methods

The accelerations to be applied to particles in an  $N$ -body simulation can be determined in many different ways that fall into two broad classes. Direct pair wise summation, usually with a tree algorithm to improve efficiency, and methods that solve for the gravitational field over a volume. Three common methods in the latter category are: (1) solving a finite difference approximation to the Poisson equation on a grid, (2) convolution between the source distribution and a Green function on a grid, and (3) expansion of the field in multipoles, with either a basis set to represent the radial part or a grid on which the contributions of interior and exterior masses are tabulated. Grid and field methods are far more efficient than tree codes, albeit at the cost of ease of use and versatility.

All grid methods assign masses to a spatial raster of points and tabulate the field at the same points. Sensible interpolation schemes to treat particles between grid points lead to forces between particles that decrease smoothly at separations below one grid space, reaching zero for coincident particles.

Finite difference methods solve an approximation to the Poisson equation directly, yielding a potential arising from the mass distribution. Acceleration components, which have to be estimated from a finite difference approximation to the gradient operator, lead to forces that approximate the full Newtonian value at distances of greater than a few mesh spaces, but which are significantly weaker at short range (*e.g.* appendix of Sellwood & Merritt 1994).

Convolution methods, on the other hand, can be used to compute the acceleration components directly, without the need to difference a potential. The Green function is the force field of a unit mass, which requires a separate convolution for each coordinate direction. However, the force law needs to be softened at short range both to prevent acceleration components from varying so steeply across a grid cell that simple interpolation rules become inadequate and also to limit the maximum possible acceleration, particularly where grid cells become very small near the centres of polar grids.

### A2 Softening Rules

Since any arbitrary softening rule can be adopted in convolution methods, physical considerations can be used to select the optimum rule for a particular application. The Plummer softening rule for a unit mass uses the density profile and potential

$$\rho(x) = \frac{3}{4\pi\epsilon^3}(1+x^2)^{-5/2}; \quad \phi(x) = -\frac{G}{\epsilon}(1+x^2)^{-1/2}, \quad (\text{A1})$$

where  $x = r/\epsilon$ , with  $\epsilon$  denoted the softening length. This rule is optimal when particles are confined to a plane, because it yields in-plane accelerations that would result if the razor-thin mass distribution were displaced vertically by the softening length. The forces can be thought of as approximating those from a disc of finite thickness since softening affects the dispersion relation for spiral waves (*e.g.* Vandervoort 1970; Erickson 1975; Romeo 1992) in much the same way as does finite thickness. We therefore employ this rule when particle motion is confined to a plane.

The disadvantage of the Plummer softening rule in 3D simulations is that it weakens forces on all scales and other rules that avoid this shortcoming have become popular. The precise short-range behaviour is of little importance for relaxation, since inverse square-law forces imply scattering is dominated by the cumulative effect of long-range encounters (*e.g.* BT08, p. 36). For our 3D simulations we adopt the somewhat clumsy cubic spline density kernel used in the original version of the tree code PKDGRAV (Stadel 2001), which has the form

$$\rho(x) = \frac{1}{4\pi\epsilon^3} \begin{cases} 4 - 6x^2 + 3x^3 & 0 \leq x \leq 1 \\ (2-x)^3 & 1 \leq x \leq 2 \\ 0 & \text{otherwise,} \end{cases} \quad (\text{A2})$$

as suggested by Monaghan & Lattanzio (1985).<sup>2</sup> The density has continuous second derivatives, while the potential is given by a messy expression at short range but is, of course, that of a unit point mass when  $x > 2$ .

### A3 Codes

For fully 3D simulations, we use the hybrid grid method described elsewhere (Sellwood 2003). It solves for the field by convolution on a 3D cylindrical polar grid for the disc particles, with the softening rule (eq. A2), while the accelerations of the halo particles are computed using method (3) of Section A1 on a spherical grid.

We also report a number of results using both polar and Cartesian 2D grids, where we use the Plummer softening law.

In most experiments, we shift the centre of both grids to a new location every 16 time steps. The new centre is location of the particle centroid (McGlynn 1984). The estimate of the change in this location is determined by Newton-Raphson iteration, which is repeated until the shift at each iteration is less than  $10^{-3}R_d$ . This process is unnecessary when any lop-sidedness in the mass distribution does not contribute to the accelerations and when Cartesian grids or tree codes are used.

<sup>2</sup> Their expression omits the square of  $x$  in the first line, but this typo is corrected in Monaghan (1992).

In addition, we have used the tree code, PKDGRAV Stadel (2001), which adopts the softening kernel  $K_1$  recommended by Dehnen (2001). We have also conducted a few tests with the numerical parameters of time step, opening angle, *etc.*, and found results with this code also are independent of these choices to a similar level of tolerance.

#### A4 Time steps

When using grid methods, we adopt a 5-zone time stepping scheme in which the more slowly moving outer particles have time steps that increase by a factor 2 from zone to zone. All particles experience forces from all others at every step, but forces from particles in outer zones are interpolated to intermediate times (Sellwood 1985).

#### A5 Measurements of $A$ and $\Omega_p$

We need to make quantitative comparisons of the bar evolution in simulations as codes, numerical parameters, or random seeds are varied. In particular, we compare the evolution of the overall amplitude and phase of a bar-like distortion in the disc. We measure this quantity by computing

$$A_2(t) = \frac{1}{N_d} \sum_{j=1}^{N_d} e^{2i\theta_j}. \quad (\text{A3})$$

where  $N_d$  is the total number of disc particles and  $\theta_j(t)$  is the azimuth of the  $j$ th disc particle at time  $t$ , reckoned from a fixed direction through the centre defined as the particle centroid at that time. Since the quantity  $A$  is complex, the bar amplitude is  $|A_2| = [\Re(A_2)^2 + \Im(A_2)^2]^{1/2}$  and phase  $2\theta_b = \arctan[\Im(A_2)/\Re(A_2)]$ , with the factor 2 appearing in order to yield a phase that increases by  $180^\circ$  as the bi-symmetric pattern makes half a rotation. We measure  $A_2$  at frequent intervals, generally every 0.1 dynamical times. The pattern speed of the bar is clearly the time derivative of the phase

We make a smoothed estimate of the amplitude and pattern speed by fitting a steadily rotating wave to the complex  $A_2$  values over a short time interval, and sliding the time interval forward to follow the evolution of both quantities. Our plots of amplitude and pattern speed are of the smoothed quantities.

## APPENDIX B: TESTS OF NUMERICAL PARAMETERS

As always, we check the extent to which the behaviour depends upon all numerical parameters. We have been particularly thorough in the case of our standard model where our results are so surprising. Since simulations with a rigid halo and the disc particles confined to a plane already show large variations (Fig. 15), we begin by presenting checks of these inexpensive simulations.

### B1 Grid Geometry

We have run these calculations on both a 2D polar grid and a 2D Cartesian grid in order to convince ourselves that our

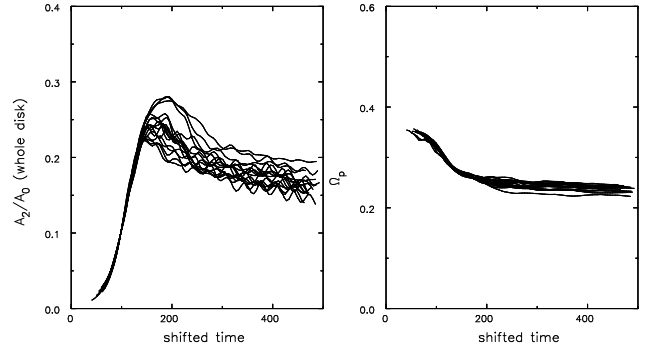


**Figure B1.** Evolution of the bar in 16 runs with different random seeds for the disc particle coordinates. These simulations use a 2D Cartesian grid: numerical parameters are as given in Table 2 except  $N_x \times N_y = 256^2$ , there is a single time step zone and the grid is not recentered.

results were not being affected by our choice of grid geometry. The result for the Cartesian grid is shown in Fig. B1, which should be compared with that for the polar grid shown in the second row of Fig. 15, for which the number of particles and softening length were identical. Again the curves for separate runs have been shifted in time so that they all pass through amplitude 0.1 at the same instant, which is the mean of the set shown.

While there are differences in detail between the two figures, the mean and spread in the amplitude evolution are quite similar.

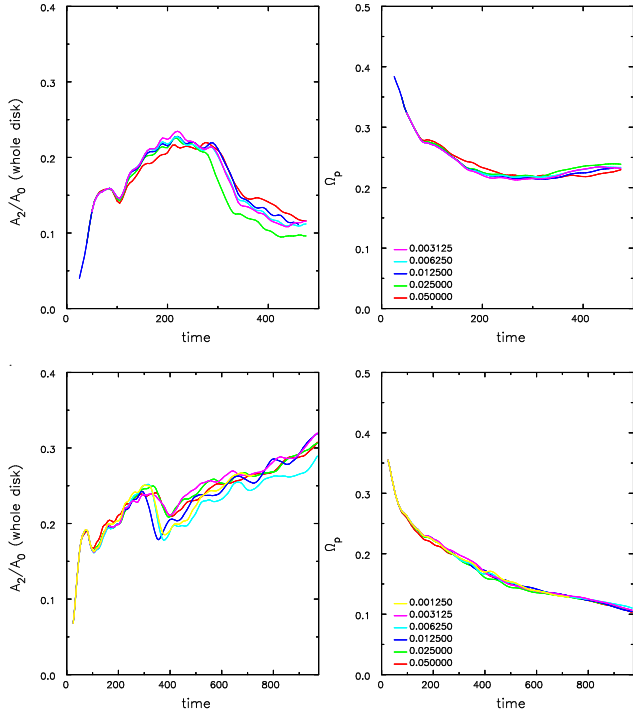
### B2 Time Step

Fig. B2 shows that changing the time step also has little effect on the evolution. These tests are for two of the 3D models shown in Fig. 4, one in which the bar slowed at late times and one in which it did not. The value of the time step parameter is varied by a factor of 40 in the case that slowed strongly. Small differences in the evolution develop at late times because the system is chaotic but the deviations do not vary systematically with the step size. If the orbital angular frequency is  $\Omega_c$ , a particle takes  $2\pi/(\Omega_c \Delta t)$  steps for a circular orbit. The central value of  $\Omega_c \simeq 2$  for our standard model, implying 250 steps per orbit for the most bound particles at our standard time-step, and ten times as many for the shortest step used in Fig. B2. In agreement with Dubinski *et al.* (2009), we therefore find no evidence to support the claim by Klypin *et al.* (2008) that these simulations require  $> 2000$  time steps per orbit period for the most tightly bound particles.

We have also verified that the evolution is similarly insensitive to using a fixed time step for all particles, instead of the more efficient scheme of employing longer steps at larger distances from the centre.

### B3 Grid Resolution

Fig. B3 shows the effects of changing the size of the cylindrical polar grid used for the disc in the hybrid code, keeping the initial particle coordinates and all other numerical parameters fixed. As in other tests, small differences in the evolution develop at late times but aside from the two coarsest



**Figure B2.** Evolution of the bar in two sets of runs with the same random seeds for the disc particle coordinates. Numerical parameters are given in Table 1 except the time step is varied. Values adopted are colour coded as shown. Upper panels show the evolution from one set of initial coordinates, lower panels from a second set.

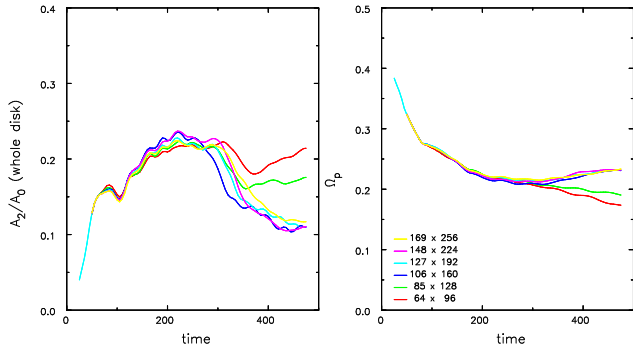


**Figure B3.** Evolution of the bar in 3D runs with the same random seeds for the disc particle coordinates using different grid sizes. Numerical parameters are given in Table 1 except the number of grid cells used for the 3D polar grid is changed, as indicated by the line colours.

grids, for which the late time evolution departs systematically from the rest, the results are quite similar. We have also found that smaller differences result when we double or halve the vertical spacing of the grid. Our standard grid (Table 1) is shown by the cyan line and seems adequate.

In addition, we checked that the evolution is unaffected (to the same level of tolerance) by changing the number of active sectoral harmonics of the polar grid to  $m_{\max} = 4$  or  $m_{\max} = 16$  from our standard value of  $m_{\max} = 8$ , or by changing the order of azimuthal expansion  $l_{\max}$  and the

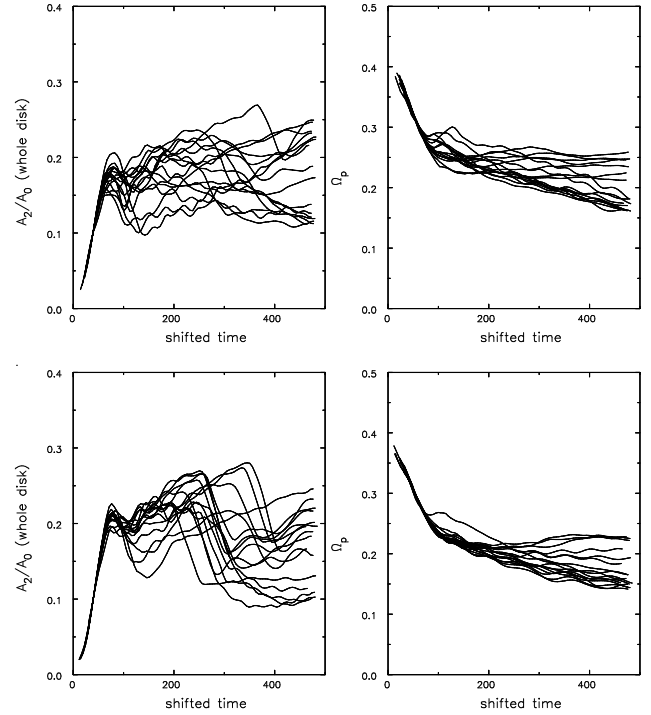


**Figure B4.** Evolution of the bar in 3D runs with the same sets of random seeds for the disc particles as in Fig. 4 but using different softening lengths. The softening length in the upper and lower panels is respectively halved and doubled from our standard value.

number of shells  $n_r$  of the spherical polar grid from our standard values of  $l_{\max} = 4$  and  $n_r = 300$ .

#### B4 Softening

Fig. B4 shows the effects of changing the softening length for force convolution on the 3D polar grid used for the disc in the hybrid code, with the initial particle coordinates and other numerical parameters unchanged from Fig. 4. As reported elsewhere (Sellwood 1981, 1983; Sellwood & Merritt 1994, *etc.*), the evolution of disc instabilities is more sensitive to this numerical parameter than perhaps any other. The growth rates of both bar-forming modes, and of bending modes are quite sensitive to the sharpness of short-range forces. The effect of a longer softening length (lower panels) is both to increase the initial peak amplitude of the bar, because the second mode is more strongly suppressed by softening than is the dominant, and to make bending instabilities occur later and more violently.<sup>3</sup> The effects of a reduction in softening are less systematic, but the extra virulence of swing-amplified shot noise is the probable cause of more marked upward fluctuations in the pattern speed evolution and there are fewer violent buckling events.

Since it is desirable to use the largest value that does not

<sup>3</sup> The reason is as follows, adapted from Merritt & Sellwood (1994): If stars move at speed  $u$  in one-dimension over a ripple of wavenumber  $k$ , then a condition for a growing bend is that  $ku < \kappa_z$ . Increasing softening reduces  $\kappa_z$ , which causes only smaller  $k$ , or longer wavelength, bends to grow.

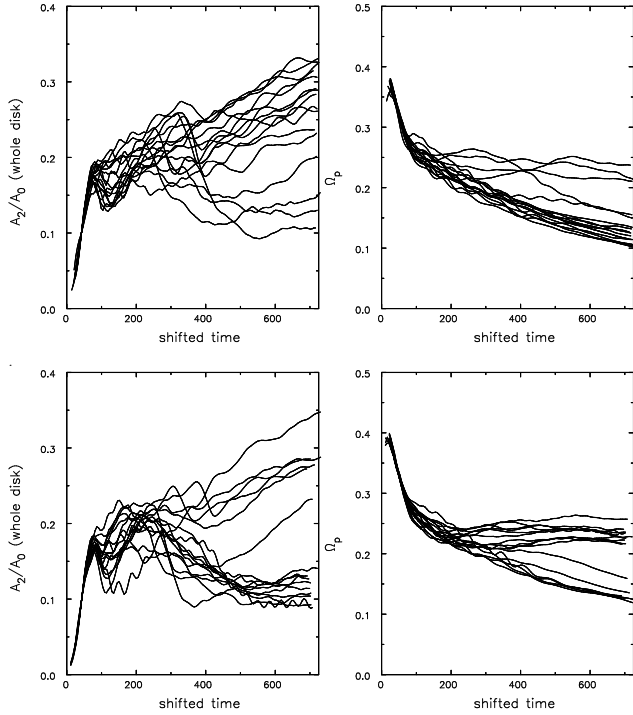


**Figure B5.** Evolution of the bar in runs to test the dependence on the number of halo particles. The upper panels used one tenth the number of unequal mass particles employed in Fig. 4, while the number employed in the lower panels was 10 million. Other numerical parameters are held fixed at the values given in Table 1.

have a systematic influence on the outcome, these tests show that our standard value seems a reasonable compromise.

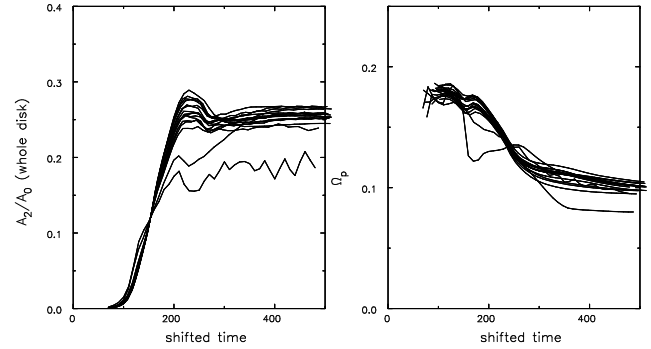
### B5 Number of Halo Particles

Fig. B5 shows two sets of runs with different numbers of unequal mass halo particles, in which the random seeds for the disc particles were changed. (We already reported the dependence of the behaviour on the number of disc particles in Fig. 15.) Again, the behaviour in these tests, and in another set with 2.5M equal mass particles, is qualitatively similar to that shown in Fig 4. The ranges of final amplitudes and pattern speeds do not depend on the number of halo particles or whether the masses are all equal. There is a trend, in that the fraction of bars that do not experience strong friction seems to increase with increasing numbers of halo particles: it is 4/16 for  $N_h = 2.5 \times 10^5$ , 7/16 for  $N_h = 2.5 \times 10^6$  (Fig. 4) and 11/16 for  $N_h = 10^7$ . For the experiments with  $N_h = 2.5 \times 10^6$  equal mass particles, the non-slowing fraction is 3/16.

We make use of this trend with the quality of the simulations in the discussion of Sections 4.2 & 6.

## APPENDIX C: EFFECTS OF PARTICLE SELECTION FOR THE ISOCHRONE DISC

Here we illustrate the advantages of careful particle selection for a simple disc model with well-defined global instabilities.



**Figure C1.** Evolution of the bar in the isochrone/8 disc, but instead of selecting particles deterministically as in Fig. 13, we used a simple acceptance/rejection algorithm. Note the larger spread in the measured bar properties.

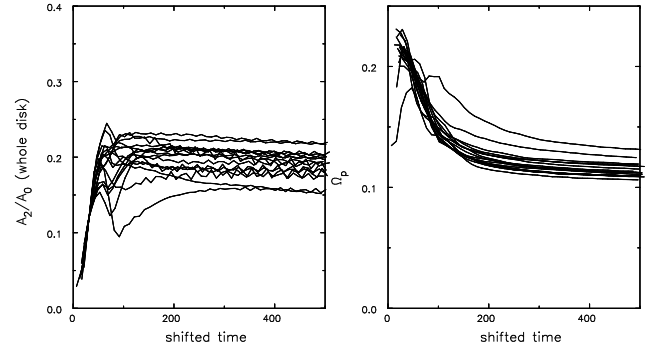


**Figure C2.** Evolution of the bar in a noisy start isochrone disc in which the non-circular motions were set up crudely rather than selecting from a DF. The value of  $Q$  in the initial disc is similar to that of the initial models in Figs. 13, 14, & C1.

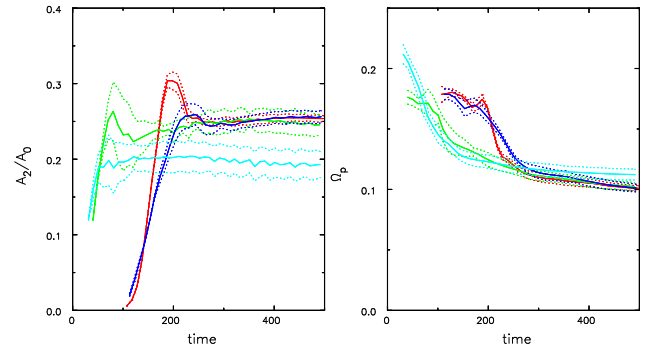


**Figure C3.** Summary of results from in Figs. 13 (red), 14 (green), C1 (blue), & C2 (cyan) in order to illustrate the ranges of scatter.

The value of a quiet start was already illustrated by comparison of Figs. 13 & 14 but particles were deterministically selected from the DF for both sets of simulations.

Fig. C1 shows the consequences of selecting particles by the commonly-used acceptance/rejection method. Even though these experiments still used quiet starts (replicas of each master particle spaced evenly around a ring), the results are less well behaved: there is more scatter particularly

in the bar amplitude, with one or two significantly anomalous results.

Fig. C2 shows the results from experiments in which the set up procedure for the random speeds of the disc particles stemmed simply from the requirement that  $Q = 1.2$  everywhere, with the azimuthal dispersion and asymmetric drift determined by Jeans equations in the epicycle approximation, as suggested by Hernquist (1993). Although this may be the most commonly used method, the outcome of such experiments shows the greatest degree of scatter.

The effects of quiet and noisy starts, and other particle selection issues are summarized in Fig. C3. Generally, experiments with noisy starts show considerably more scatter than do those with quiet starts, and deterministic selecting from a DF is superior to random sampling or not using a DF at all.